Defense Technical Information Center
Compilation Part Notice

ADP010745

TITLE: The VKI Plasmatron Characteristics and
Performance

DISTRIBUTION: Approved for public release, distribution unlimited

This paper is part of the following report:

TITLE: Measurement Techniques for High Enthalpy
and Plasma Flows [Techniques de mesure pour les
ecoulements de plasma et les ecoulements a haute
enthalpie]

To order the complete compilation report, use: ADA390586

The component part is provided here to allow users access to individually authored sections
of proceedings, annals, symposia, ect. However, the component should be considered within
the context of the overall compilation report and not as a stand-alone technical report.

The following component part numbers comprise the compilation report:

The VKI Plasmatron Characteristics and Performance

B. Bottin, O. Chazot, M. Carbonaro, V. Van Der Haegen, S. Paris
The von Kármán Institute for Fluid Dynamics
72 Chaussée de Waterloo
B-1640 Rhode-Saint-Genèse
Belgium

Abstract

The von Kármán Institute (VKI) recently completed the commissioning of a new inductively-coupled plasma wind tunnel ("Plasmatron") devoted to the simulation of thermal re-entry conditions as applicable to TPS materials used on real flight trajectories. In the context of the commissioning, two main intrusive measurement techniques, the Pitot tube and the calorimetric heat flux probe, were developed and extensively used to record the performance in order to compare them with the specifications. During the commissioning phase, other techniques were being developed in another VKI facility, the Minitorch, a small inductively-coupled plasma torch used as the instrumental test bench for the Plasmatron. This paper presents the Plasmatron facility to the reader, then describes in detail the probes that were used, the test methodology that was followed, and the results that were obtained during the commissioning phase. The technique of laser Doppler velocimetry (LDV), which is currently developed in the Minitorch and envisaged as one of the standard Plasmatron techniques in the near future, is also described in detail.

1. The Plasmatron facility

1.1 Inductively-coupled plasma heaters

The concept behind plasma generation by induction is sketched on figure 1. A coil surrounds a quartz tube in which cold gas is injected. This coil is connected to a high-frequency generator and is traversed by high-voltage, high-frequency current (a few thousand volts with frequencies from 400 kHz to several MHz).

Due to these conditions, induced electric and magnetic fields exist inside the quartz tube, with induction lines parallel to the axis, as in a classical solenoid. The periodic time variation of the induction creates circular, oscillating electric fields in planes perpendicular to the tube axis. These fields can move the free electrons existing in the gas, creating current loops (*eddy currents*) heating the gas by Joule effect. Once the gas heats up, it dissociates and

ionises into a plasma. Conceptually, the torch is actually a transformer (as illustrated on figure 2), with the coil as primary winding and the induced current loops in the gas as secondary windings.
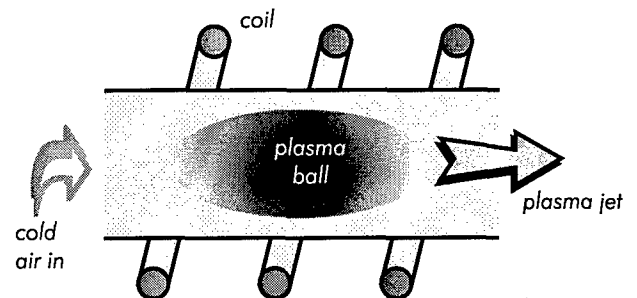

Figure 1. Concept of the inductively-coupled plasma torch

The first free electrons can be obtained by introducing an electrode into the plasma torch or, preferably, by reducing the pressure under 0.1 mbar and applying voltage on the coil. Electric field gradients appearing in the vicinity of the coil (between turns) are strong enough to cause a local ionisation of the gas in the tube. Once the first free electrons have appeared, the whole gas is rapidly heated by Joule effect. Argon is used in order to facilitate the initial electric discharge because of the longer lifetime of the free electrons at low pressure compared to the air plasma case. By these means plasma can be generated from low to atmospheric pressures with temperatures of the order of 6000 K to 12000 K. The operation of such ICP devices can be maintained as long as desired, provided that electricity, gas supply and adequate cooling are not interrupted.

1.2 Motivation and requirements

The Plasmatron project was originally devised towards the end of 1992 as part of the European Hermes reusable space vehicle programme, and later became part of the MSTP (Manned Space Transportation Programme) research program of the European Space

Agency. Indeed, future European space missions have brought the need of specific tools for the development and testing of new thermal protection systems within Europe. As presented above, no ICP facility of high power was available in Europe to satisfy those needs. This fact led, towards the end of 1994, to the financing by ESA and the Belgian Federal Office for Scientific, Technical and Cultural Affairs (OSTC) of the design, fabrication and assembly of a 1.2 MW Plasmatron at the VKI. This facility is, at the present time, the most powerful of its kind in the world. It was inaugurated on December 8, 1997 by Belgian Minister Yvan Ylieff and by the ESA Director of Manned Space Flight and Microgravity, Jorg Feustel-Buechl.
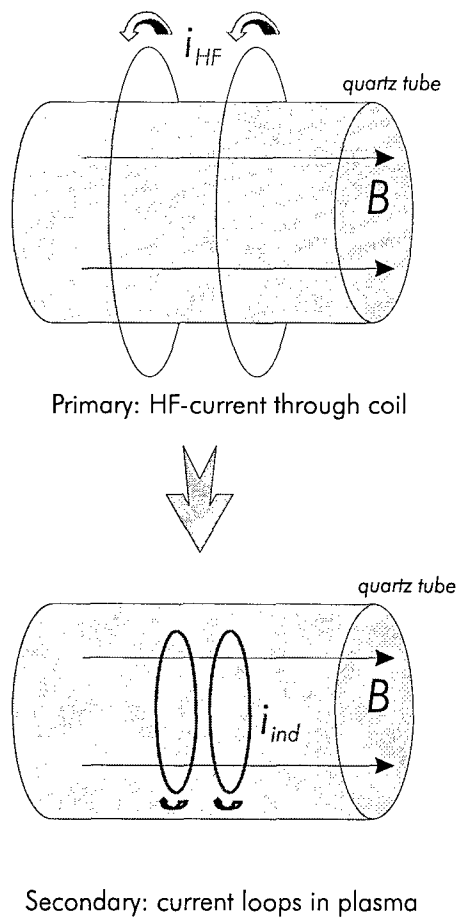

Figure 3. ESA specifications diagram for the VKI Plasmatron

1.3 The Plasmatron facility

1.3.1 The ICP torch

The ICP torch designed for the Plasmatron facility is of the latest double flux cold crucible technology. Its principle is illustrated on figure 4. Compared to the basic design (figure 1), the torch features an additional quartz tube, located inside the outer tube, which serves to divide the gas between central and peripheral injections. The purpose is explained below.

Primary: HF-current through coil

Secondary: current loops in plasma

Figure 2. The inductively-coupled plasma torch seen as a transformer

Figure 4. Concept of the double flux, cold crucible, ICP torch

The specifications for the facility are matched to the flight envelope of the Hermes vehicle (although the project was abandoned, it is a good representative of a typical lifting re-entry). They are given in terms of stagnation point heat flux and stagnation pressure, as shown on figure 3. It must be noted that the heat flux rates have to be reached on a catalytic cold wall in order to avoid uncertainties due to catalytic effects. This operating envelope has been achieved during the commissioning phase of the facility, as will be presented later.
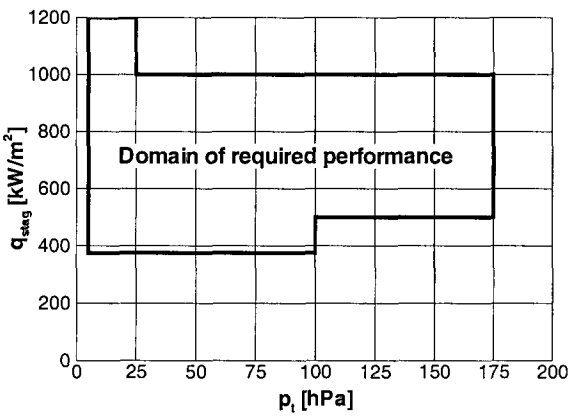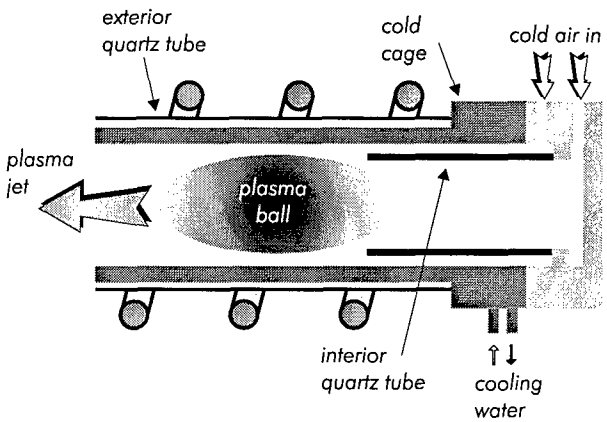
It is understandable from the basic principle of an ICP torch that the plasma ball remains in the centre of the tube, confined by electromagnetic forces. However, in some conditions, the ball could expand and touch the wall, melting the quartz tube. To prevent this, a thin layer of cold air flows along the inner side in the discharge region. This peripheral gas flux shields the tube wall and feeds the plasma ball. The inner tube is used to bring the flow close to the discharge. It is thus also close to the plasma ball and may sometimes be in direct contact. The central gas flux is used to push the plasma ball away from the inner tube [1]. The fine tuning of these two injections is essential to obtain a stable plasma with relatively high-power.

Inside the torch is inserted a cold cage made of water-cooled copper segments, which serves as an additional protection for the quartz tube. One might think that the copper cage could be a source of flow pollution. However, the presence of metallic parts is a necessary but not a sufficient condition for erosion. Since the copper cage is water-cooled to a wall temperature less than the boiling point of water, there simply cannot be a direct contact between the copper and the hot plasma (otherwise the copper cage would overheat, melt and be destroyed, preventing continuous operation).

Figure 5 shows a picture of the ICP torch in operation, with the plasma glow showing through the segments of the copper cage. This segmentation is necessary to avoid screening of the high-frequency electric field by Faraday cage effect. The single-turn inductor (made of seven parallel rings) with internal water cooling can clearly be seen on the photograph. The tubes on the left provide gas supply, those on the right are used to inject cooling water into the cold cage and other parts of the metallic casing enclosing the ICP torch.
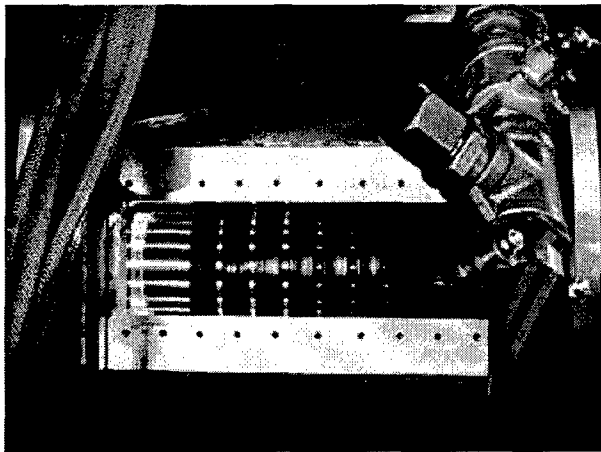

Figure 5. The Plasmatron ICP torch in operation

1.3.2 The facility

The complete Plasmatron facility schematic [2] is sketched in figure 6. It is equipped with two interchangeable ICP torches, one of 80 mm diameter for the test of small samples and one of 160 mm diameter suited to samples as well as to full TPS tiles. Each torch is mounted inside a support casing, which is fixed on a side of the test chamber, a 2.5 m long, 1.4 m diameter vessel (figure 7) equipped with multiple portholes and windows to allow maximal flexibility and unrestrained optical access for plasma diagnostic techniques.

Inside the test chamber, the samples and probes are supposed to be mounted on a three-axis fast-injection and support system. However, this subsystem is not yet operational at the present time. Instead, probes can be mounted on a traversing mechanism fixed on a porthole. Up to now, low speed plasma jets have been generated

(figure 8 shows an air plasma jet from the 80 mm diameter torch). Accelerated subsonic flows and supersonic flows will be obtained in the near future by insertion of nozzles at the outlet of the torch.
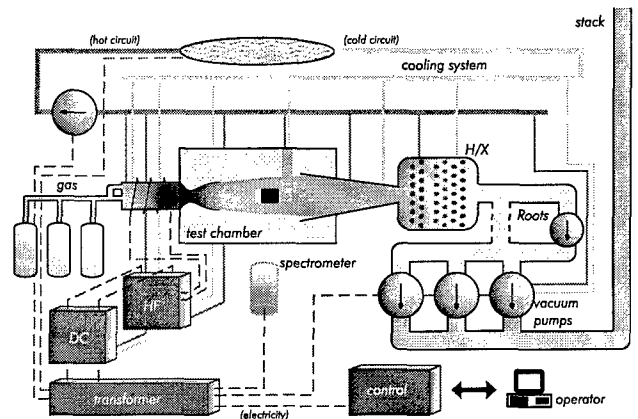

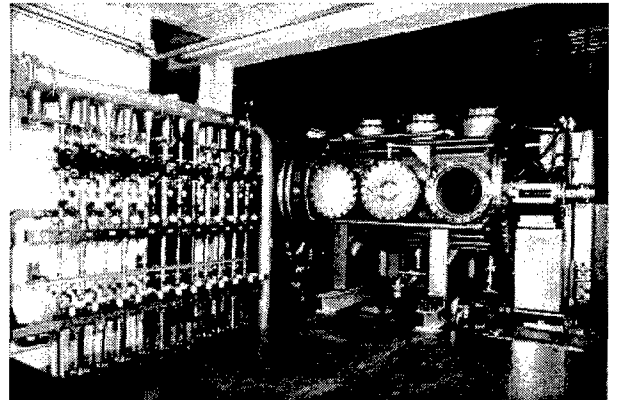Figure 6. The Plasmatron facility (schematic drawing)

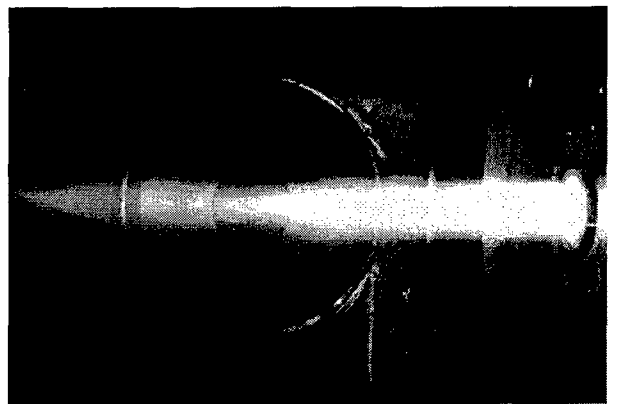Figure 7. The Plasmatron viewed from the left

Figure 8. Air plasma jet from the 80 mm torch

The jet of plasma is collected at the outlet of the test chamber and cooled in the heat exchanger to a temperature of 50 °C to protect the vacuum plant from overheating damage. Figure 9 shows the heat exchanger vessel, which is as big as the test section. Inside are two modules, each with its own cooling line. The front

module has two rows of 28 tubes and faces the maximal heat load from the jet. The back module has 16 rows of 28 tubes, with the last 14 rows made of flattened tubes in order to reduce the pressure loss. The vacuum plant consists of three volumetric vacuum pumps which allow operating pressures between 1 hPa and atmospheric pressure with a maximum flow rate of 3000 m³/h. A Roots pump can be inserted in the circuit to bring the pressure down to 4 Pa without any volume flow penalty. Exhaust gases are vented to the atmosphere through a stack.
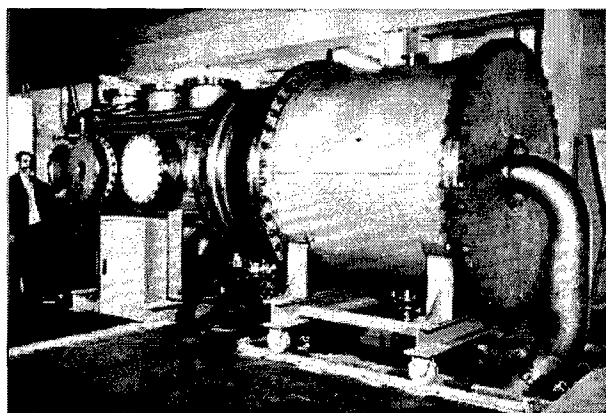

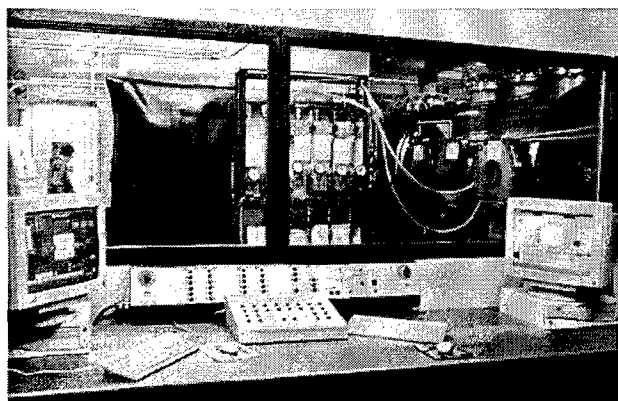*Figure 9. The Plasmatron viewed from the right*

Figure 10. The Plasmatron viewed from the control cabin

The Plasmatron is equipped with a 1.2 MW, 400 kHz, high-frequency generator of the new solid-state technology, using thyristors and MOS inverters instead of vacuum tubes. A closed circuit cooling system using de-ionised water protects all facility parts from melting due to the plasma heat, which is evacuated through three dry air coolers located on the roof. The total water flow rate is about 2088 l/min. Figure 7 shows the individual cooling lines and the collection manifold. The working pressure of this cooling system is 3 bar, but specific cooling lines (inductor, copper cage and test probes) are fed at a 10 bar pressure to compensate for the very small size of internal cooling passages encountered within the subsystems. Test gases can be injected from carboys in order to duplicate the required chemical composition. A separate carboy provides argon for ignition purposes. For air plasma, the facility is connected to the VKI compressed air supply.

The full facility is computer-controlled from a remote cabin. Figure 10 shows the facility as seen from the control cabin, with the gas supply panel in the background.

2. Performance measurements

2.1 Introduction

The performance matrix imposed by the European Space Agency (figure 3) needed to be experimentally confirmed by performing total pressure and heat flux measurements. To that effect, specific probes have been designed, built and used. However, the probes allow to obtain much more information than simply the values of total pressure and heat flux. Coupled with a specific data reduction procedure, the experimental results can be used to obtain significant information on the flow.

The data reduction procedure cannot be applied without some model of the plasma state. It requires the use of several numerical tools, as outlined on figure 11. These models include of course adequate thermodynamic and transport properties modules, the input from the measurements, and a stagnation-point heat transfer computation. This module is the most sensitive as far as data reduction is concerned, because the capability to relate stagnation properties to flow properties directly depends from the quality of this module.
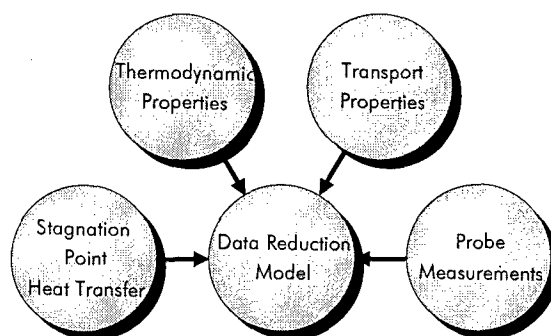

Figure 11. Elements to take into account in the data reduction model of the Pitot and heat flux probes measurements

2.2 The Pitot probe

2.2.1 Description

The Pitot probe used in the Plasmatron is similar to classical Pitot probes, except that it is water-cooled to resist the plasma heat. It is made out of brass and has a hemispherical head of 12 mm diameter, with a pressure-sensing orifice of 2 mm diameter. The size of the Pitot is imposed by the requirements of installing the water passages for the water. The design of the

probe has been inspired by the example of the Pitot probe used in the LBK arc-jet facility at DLR Köln. The conceptual drawing of the Pitot probe is shown on figure 12 and a picture of the probe is shown on figure 13 [2]. The probe is connected to the Plasmatron cooling system and receives water at a pressure of 10 bars and a flow rate of 8 l/min.
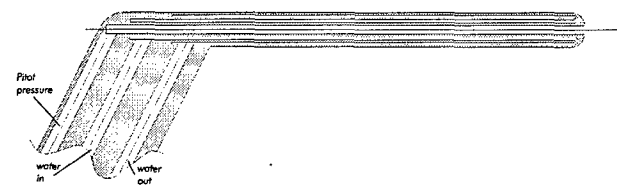
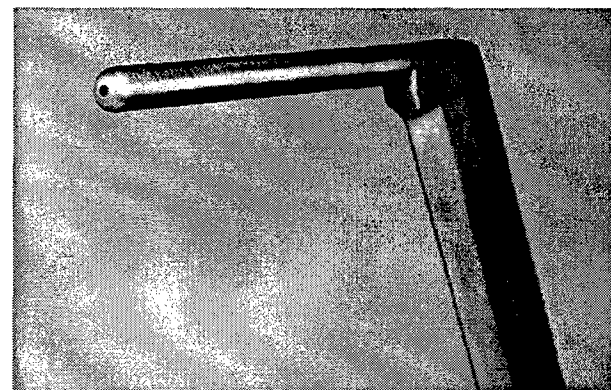

Figure 12. Conceptual drawing of the Pitot ptobe

Figure 13. The Pitot probe as built

2.2.2 Measurements and accuracy

The Pitot probe is used to perform stagnation pressure measurements. The required experimental set-up is shown conceptually on figure 14. The static pressure p_s of the Plasmatron chamber is measured by an absolute pressure transducer of 0.3% full-scale uncertainty (Leybold ceramic capacitance diaphragm transducer DI200). The Pitot tube is connected to a differential pressure transducer (Valydine variable reluctance transducer DP45), calibrated using a Betz precision micro-manometer. The transducer output is read on a pen plotter.
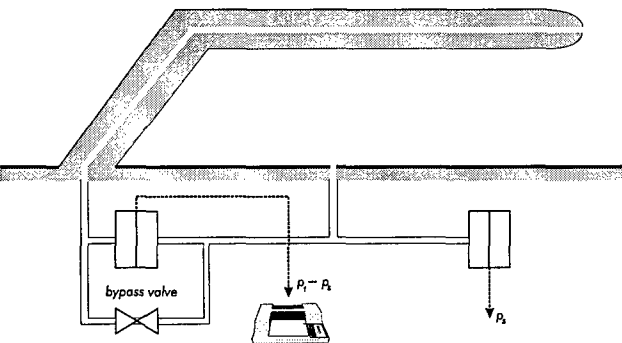

Figure 14. Pitot pressure measurement set-up (schematic drawing)

The accuracy of each component is indicated on table 1 according to the manufacturer's specifications (reading accuracy is assessed based on the capability of the user to distinguish half of the interval between two lines on the plotter paper). The global error can be obtained either by summing up each error ("highest error possible" approach) or by using the square root of the sum of the squares of the successive errors ("most probable error" approach). We obtain:

- Final absolute error on the static pressure:
  $\Delta p_s = 0.6$ hPa.
- Final absolute error on the Pitot differential pressure reading: $\Delta(p_t - p_s) = 0.022$ hPa (most probable).
- Final absolute error on the Pitot pressure:
  $\Delta p_t = 0.6$ hPa (most probable).

Component	Quoted uncertainty	Absolute error
Plasmatron transducer DI200	0.3 % on 200 hPa	0.6 hPa
Validyne pressure transducer	0.25 % on 86 mm H_2O	0.021 hPa
Betz micro-manometer	0.02 mm H_2O	0.002 hPa
Pen plotter	0.3 % on 1 V (10 inches)	0.003 hPa
Reading accuracy	0.05 inches	0.005 hPa

Table 1. Uncertainty of the Pitot probe measurement chain

2.3 The heat flux probe

2.3.1 Working principle

The heat flux measurement is carried out by heat balance between power inflow from the plasma and power outflow through the cooling water:

$$q\,S = \dot{m}\,c_p\,(T_{out} - T_{in}) \qquad (1)$$

In this equation, the left side represents power brought from the plasma jet into the probe, with q the stagnation-point convection heat flux rate (unknown) and S the area of the sensing element. The right side represents power evacuated by the cooling circuit of the probe, with $\dot{m}$ the mass flow rate of the water and c_p its specific heat. T_{in} and T_{out} are the water temperatures at respectively the inlet and outlet of the sensing element.

2.3.2 Description

The heat flux probe has been specifically designed at VKI [3]. Its concept is shown on figure 15. The probe is shaped exactly as the standard TPS sample holder of the European Space Agency, so that the stagnation-point velocity gradient at the edge of the boundary layer can be the same in both cases (hence, there is no change
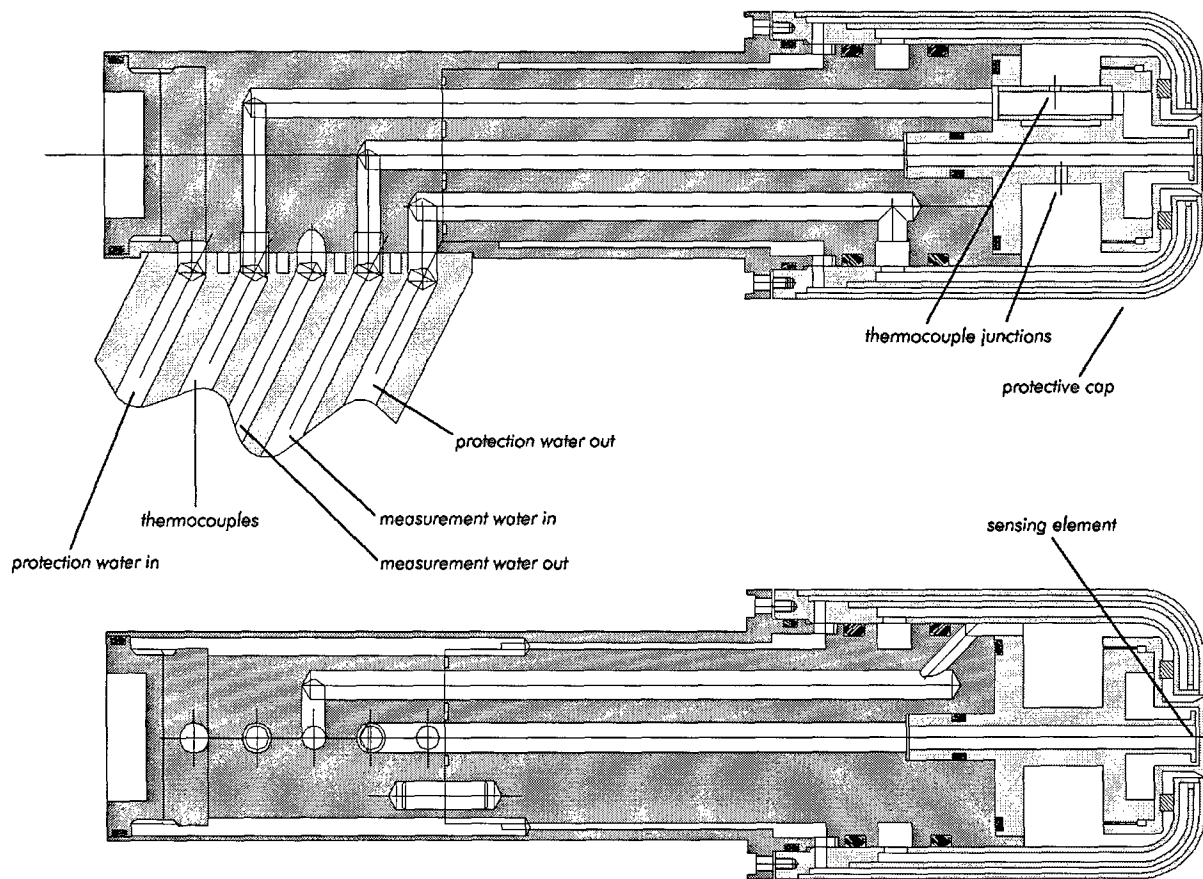
Figure 15. Conceptual drawing of the heat flux probe

in heat flux due to the geometry). The front part of the probe is made of copper, which is a highly catalytic material and is used as a reference material in many facilities. The sensing element is 14 mm in diameter. Cold water flows against its inner wall, coming from the probe centreline. A thermocouple junction is inserted to measure T_{in} close to the sensing element. Water flows radially outwards and is mixed in the collector before flowing back into the stem. Another thermocouple junction is inserted after the collector to measure T_{out}.

The external shape of the probe is obtained by the protective cap, in which cold water is also flowing to avoid damage by the plasma flow. This protective cooling water circuit is completely separated from the measurement circuit (the water is taken from the Plasmatron cooling system at 10 bar and 10 l/min). The external wall of the cap is made of copper as well, in order to avoid changes in wall catalycity around the sensing element (such differences in wall catalytic properties can cause local heat flux overshoots of 10% [4] that perturb the measurements considerably). There is a small gap between the sensing element and the cap, to avoid contact causing heat losses by conduction. As a consequence, the interior space around the sensing element is under the same low pressure than the Plasmatron chamber. This increases the insulation between the sensing element and other parts of the probe.

2.3.3 Measurements and accuracy

Figure 16 shows the measurement chain required for the measurement of heat flux rate. The two thermocouple junctions measuring the temperature difference are part of the same thermocouple. The signal then directly gives a measure of the temperature difference $(T_{out} - T_{in})$. Besides a greater accuracy (it eliminates the need of calculating a small difference between two large quantities), doing so also removes the need of compensating wires.
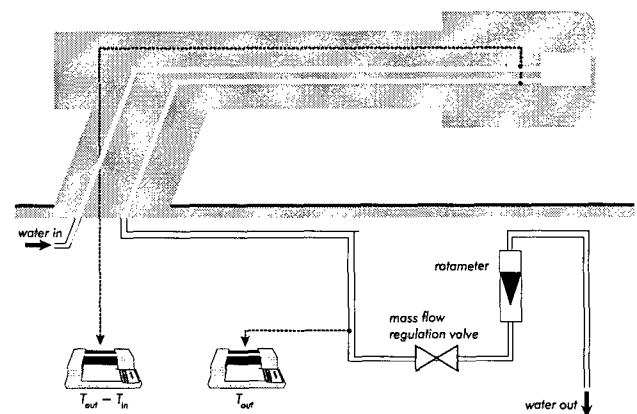

Figure 16. Heat flux measurement set-up (schematic drawing)

Another thermocouple is installed to measure the water temperature in the measurement circuit at the exit of the probe, where the mass flow rate has to be measured. A rotameter is used to measure the mass flow rate, which can be adjusted manually by a regulating valve (changing the amount of mass flow changes the temperature difference at a given heat flux rate). Both temperature records are made using a pen plotter. The mass flow determination from the rotameter float height involves reading the calibration curves provided by the manufacturer. In order to obtain reduced processing times, a small computer program was written to interpolate the calibration curves automatically, in such a way that no additional error is performed.

From (1) it is seen that the accuracy depends on the mass flow measurement, temperature difference measurement and sensing element area (neglecting uncertainties on the water c_p). The uncertainties associated with the individual elements of the measurement chain are given by table 2 and can be combined using classical error analysis, to give a highest error of:

$$\frac{\Delta q}{q} = \frac{\Delta S}{S} + \frac{\Delta (T_{out} - T_{in})}{T_{out} - T_{in}} + \frac{\Delta c_p}{c_p} + \frac{\Delta \dot{m}}{\dot{m}} \qquad (2)$$

and a most probable error of:

$$\frac{\Delta q}{q} = \left[\left(\frac{\Delta S}{S}\right)^2 + \left(\frac{\Delta (T_{out} - T_{in})}{T_{out} - T_{in}}\right)^2 + \left(\frac{\Delta c_p}{c_p}\right)^2 + \left(\frac{\Delta \dot{m}}{\dot{m}}\right)^2\right]^{1/2} \qquad (3)$$

The value of heat flux involves many variables and a value of uncertainty cannot be obtained in such a straightforward way as was done in the Pitot probe case. In particular, the measurements of temperature and mass flow rate are related: if the mass flow rate increases, the temperature difference decreases, and so the error on the former decreases but the error on the latter increases.

More in-depth error analysis requires to examine the actual operating conditions of the heat flux probe in the plasma flow. As is shown by figure 17, pen plotter recordings of the temperature show high-frequency oscillations. When the mass flow is too small (e.g. 60 mm float height – 4.3 g/s), the oscillations are big. They first decrease with increasing mass flow (e.g. 70 mm, 5.4 g/s) then increase again (not shown). In the example, the oscillations at 70 mm and 80 mm (6.4 g/s) are comparable in amplitude, but the mean signal was steadier at 70 mm. Of course, as the mass flow rate increases, the temperature difference decreases, so the height of 70 mm was chosen, except when the heat flux was too high, in which case the mass flow was increased.

This behaviour could be interpreted as follows: at low mass flow, the flow is laminar; as it increases, the flow can get turbulent in the sensing element of the probe, causing greater oscillations in the output traces. Consequently, increasing the mass flow causes an increase in signal noise. The decrease in signal noise which is first

observed when the mass flow is increased can indicate that, when the mass flow is too low, the convection coefficient is not high enough to prevent local boiling of the water. The bubbles will cause signal noise when passing over the thermocouple.

Component	Quoted uncertainty	Absolute error
Rotameter	1.6 % full scale	$0.37 \; 10^{-3}$ kg/s
Sensing element area	1/10 mm on diameter	$8.83 \; 10^{-6}$ m^2
Water specific heat	0.1 J/(kg K)	0.1 J/(kg K)
Thermocouple coefficient	1 %	0.25 K
Pen plotter (ΔT)	0.3 % on 1 V (10 inches)	0.075 K
Pen plotter (T)	0.3 % on 1 V (10 inches)	0.15 K
Reading accuracy (ΔT)	0.05 inches	0.125 K
Reading accuracy (T)	0.05 inches	0.25 K

Table 2. Uncertainty of the heat flux probe measurement chain.
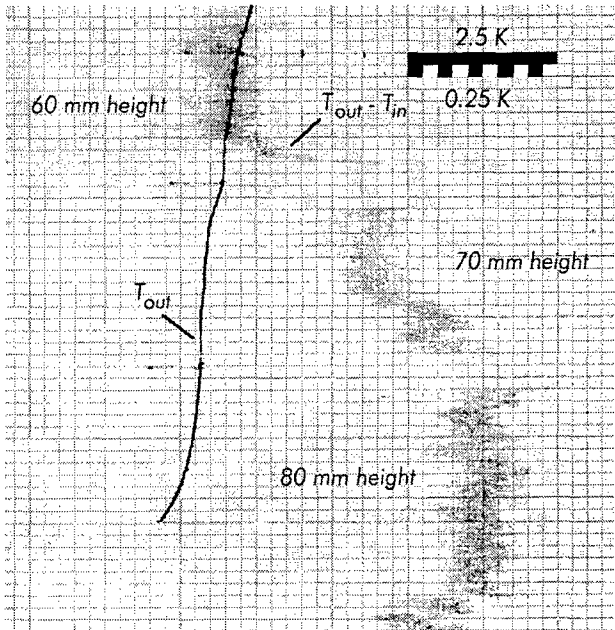

Figure 17. Typical traces recorded when the heat flux probe is in the plasma jet

The probe study that was performed[1] [3] has allowed to obtain a relationship between the mass flow rate in the probe and the heat flux rate:

[1] Numerical simulation of the flow inside the sensing element have been performed to obtain the Nusselt-Reynolds relationship for the particular geometry.

$$m = \frac{\pi \, \mu_{in} \, D_{in}}{4} \left(\frac{\frac{q \, D_{in}}{\lambda_{wall} \, (T_{wall} - T_{in})} - 5.848}{2.047 \left(\frac{\mu_{wall}}{\mu_{in}} \right)^{-0.1}} \right)^2 \qquad (4)$$

with λ_{wall} the wall thermal conductivity. Based on a wall temperature equal to the boiling point at 10 bar (440 K), the minimum mass flow rate necessary to avoid boiling is obtained. In the range of the Plasmatron original specifications, i.e. heat flux values up to 1200 kW/m², the minimal mass flow rate was compatible with values yielding significant temperature differences (about 15 K at 1200 kW/m²). As the next chapter will show, the Plasmatron performances quite exceed the original specifications. Because the necessary mass flow rate varies with the square of the heat flux, the mean temperature increase $(T_{out} - T_{in})$ varies as the inverse of the heat flux and drops down to values much too small to be of practical use. For this reason, the probe was used with lower mass flow rates, corresponding to risks of boiling in the probe. It is known that a small amount of boiling causes *nucleated boiling*, a condition that increases the local convective heat transfer coefficient. Apparently, up to the maximal measured heat flux of 3.5 MW/m², the DNB point[2] has never been reached in the performed experiments (if not, damage to the probe would certainly have occurred). However, the presence of bubbles in the flow creates additional noise on the measurement signals.

Typical conditions can therefore be identified as: mass flow rate, 6 g/s and temperature difference, 10 K. Using these values in the error assessment formulas, one gets:

- most probable relative error: $\frac{\Delta q}{q} = 8.9 \%$

2.4 Uncertainty due to the fluctuations of the measurements

As shown by figure 17, the traces recorded by the pen plotter show a high-frequency variation of the measurements. This is related, as already discussed, to the nature of the flow inside the probe, but is also related to the fluctuations of the facility operating conditions. The uncertainty of the measurements must take this phenomenon into account. In order to do so, the standard uncertainty assessment procedure used at VKI (Kline & McClintock, [5]) has been applied.

Pen-plotter records of a heat flux traverse have been used. The mean value of the heat flux has been recorded at

---

[2] *Departure from Nucleated Boiling*, when the gas phase settles in a film flowing close to the wall, forming an insulation layer that causes a severe drop in the heat transfer coefficient (a condition known as *film boiling*).

each 1 mm interval, by locating the minimal and maximal value of the high-frequency temperature variations around the sampled time position, and taking the middle value of the interval. This has been converted to heat flux. The reference heat flux value has then been taken as the mean value of all the means. An uncertainty band of ± 4.07% can be obtained for the bulk of the measurements (20 to 1 odds). Combining this uncertainty with the instrumental error of the heat flux measurements, one finally obtains a most probable relative error of 9.8 % (20 to 1) on the heat flux.

The same kind of studies have also been made for the Pitot probe. The uncertainty band is found to be 2.05 Pa (20:1). This uncertainty band can be coupled with the instrumental uncertainty determined above, to yield final values of the uncertainty:

- Most probable absolute error on the Pitot pressure reading: $\Delta(p_t - p_s) = 0.03$ hPa (20 to 1).

- Most probable absolute error on the Pitot pressure: $\Delta p_t = 0.6$ hPa (20 to 1).

2.5 Correctness of heat flux measurements

The heat flux probe yields a measurement of the heat flux received at the stagnation point, with an accuracy of about 10% based on the errors and uncertainties of the measurement chain. However, the question of the correctness of this result remains to be addressed. In other terms, how accurate is the measurement with respect to the real heat flux yielded by the flow?

2.5.1 Heat flux balance on the probe

The principle of the heat flux probe relies on a steady-state equilibrium of heat fluxes at the stagnation point: the probe is subject to the convective heat flux q_f from the flow, which can be split into the radiated heat flux q_r from the probe surface, the transmitted heat flux q_c conducted through the probe wall and the conduction losses q_l to the probe sides. The measured heat flux corresponds to q_c, and hence has a value equal to:

$$q_c = q_f - q_r - q_l \qquad (5)$$

The radiated heat flux is that of a black body surface at a temperature which cannot exceed the boiling point of water at 10 bars, i.e. 440 K. Hence, one obtains:

$$q_{r,max} = \sigma T^4 = 2125.4 \text{ W/m}^2 \qquad (6)$$

The radiated heat flux is equal to 0.6% of the minimal heat flux requirement of 350 kW/m². Hence, the radiated heat flux is negligible.

The lateral conduction losses in the probe are much limited by the gap which lies between the sensing element and the protective cap. This gap creates a layer of low-pressure air which acts as an insulator with respect to lateral heat flux losses.

Another source of conduction losses would be heat travelling in the outer walls of the sensing element. However, the mechanical design of the sensing element is such that these walls are in contact with the cooling water over several diameters before the outlet temperature is measured (figure 15). Therefore, it can be safely assumed that all the incoming heat flux has been absorbed by the water before the temperature measurement is made.

2.5.2 Outlet temperature measurement

Another source of error can come from the outlet temperature measurement in the sensing element. Indeed, numerical simulations of the first design [3] had shown that there was a significant temperature gradient at the thermocouple junction, meaning that the measured outlet temperature could be different than the mean outlet flow temperature. The design has been accordingly modified to include a mixing chamber before the outlet flow passes in the measurement region, in order to reduce this source of error to maximum extent.

3. Data reduction procedure

3.1 Thermodynamic and transport properties model

In the temperature and pressure range of ICP torches (i.e. $T < 15\ 000$ K and $p < 1$ atm), air dissociates and ionises, giving rise to a mixture of chemically-reacting thermally perfect gases which can be accurately described by the 13-species model (O_2, O, O^+, O_2^+, N_2, N, N^+, N_2^+, NO, NO^+, Ar, Ar^+, e^-) [6]. Bottin, Vanden Abeele and Barbante have developed an efficient computer library called PEGASE, used to compute thermodynamic and transport properties of arbitrary mixtures [7]. As indicated by figure 18, it is made of three modules which can be individually called from any CFD application that requires it, such as the program performing the data reduction procedure described in the present notes.

The thermodynamic module computes the thermodynamic properties of individual species using the statistical thermodynamics relations for atoms and harmonic or anharmonic oscillator diatomic molecules. It computes the equilibrium composition of the mixture using the law of mass action, through an efficient algorithm solving the system in a partly analytical, partly numerical (Newton) approach. The mixture properties are obtained from the species properties and the composition.
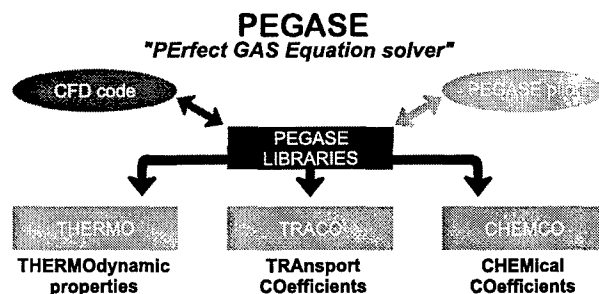

PEGASE
"PErfect GAS Equation solver"

Figure 18. Constituents of the thermodynamic model PEGASE

The transport properties module uses the kinetic theory of gases to compute viscosity, thermal conductivity and diffusion in the mixture. It relies on recent values of collision integrals data and includes second-order treatment of the electron properties and rigorous computation of both the ambipolar diffusion and the reactive thermal conductivity through the Stefan-Maxwell equations.

The chemical kinetics module produces the source terms arising from the finite-rate chemistry air models available in the literature. It is not used in the present data reduction procedure, since we are assuming local thermodynamic equilibrium.

3.2 Low-Reynolds correction to the measured Pitot pressure (Barker effect)

At very low Reynolds numbers, it is no longer possible to ignore the effects of viscosity. The radial velocity gradient close to the stagnation point causes momentum to be transferred to the stagnation streamline from the neighbouring streamlines. This leads to an increase of total pressure in the stagnation point with respect to the ideal, isentropic deceleration case. This effect[3] appears for Reynolds numbers lower than 1000, based on the external Pitot tube diameter, but only becomes significant under $Re = 100$. The increase of Pitot pressure is usually expressed as a function of the dynamic pressure of the flow:

$$C_p = \frac{p_{Pitot} - p}{\frac{1}{2}\rho U^2} \qquad (7)$$

This pressure coefficient depends of the Pitot tube shape, as clearly shown on figure 19, taken from [8]. All Pitot probes used by the various researchers had a cylindrical geometry with a flat end facing the flow. Only Pitot tube B had a round nose and yields data of interest for the present probe.

---

[3] Named according to its discoverer, M. Barker (1922).

The geometry is not exactly similar, however, since Sherman used source-shaped probes but no hemispherical probes [9]. Nevertheless, he obtained results which could be well fitted with Homann's theoretical calculations [10] for a sphere. The expression obtained by Homann almost exactly fits the data labelled B. Given the high value of viscosity and the low value of density in the plasma, the Barker effect obviously needs to be taken into account.
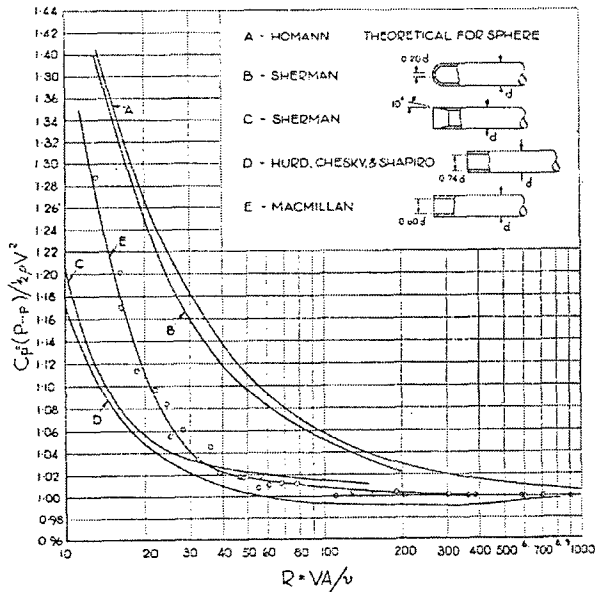

Figure 19. Pitot pressure correction for Barker effect as a function of Reynolds number and Pitot probe shape (from [8] - A = tube external diameter)

Homann's computation yields the following correction term for incompressible Barker effect:

$$p_t = p_{Pitot} - \frac{1}{2} \rho U^2 [C_p(Re) - 1] \qquad (8)$$

with

$$C_p = 1 + \frac{6}{Re + 0.455 \, Re^{1/2}} \qquad (9)$$

where the Reynolds number is expressed in terms of the probe nose radius R:

$$Re = \frac{\rho \, u \, R}{\mu} \qquad (10)$$

We cannot be sure that this relation holds true even for low-velocity plasmas, because of the density variation due to temperature. However, it is the only existing relation that we found in the literature and which offers a sound theoretical basis. More in-depth studies of the Barker effect in plasma flows may be necessary to improve the correction.

3.3 Exact computation of the stagnation point heat transfer

3.3.1 Introduction

The exact solution of the stagnation-point heat transfer on the heat flux probe can be obtained through the numerical integration of the compressible axisymmetric boundary layer equations for chemically-reacting gas mixtures. It is important, for such problems, to understand the effect that wall catalycity can have on the solution.

Figure 20 shows the difference between a non-catalytic and a fully catalytic surface. In the former case, the speed with which dissociated species recombine at the surface (noted k, catalytic recombination speed) is zero. Consequently, there is no reaction taking place on the surface. In the latter case, that speed tends to infinity and the dissociated species will recombine at the surface. In so doing, they free up their formation energy, which goes into the wall. Thus, as wall catalycity increases, the conductive heat transfer is increased too, and so is the equilibrium surface temperature.
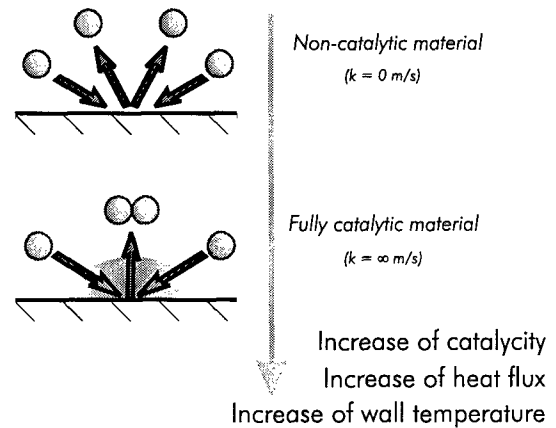

Figure 20. Effect of surface catalycity on heat flux

3.3.2 The limiting solutions: equilibrium and frozen boundary layers

Three limiting solutions can be of interest. The frozen boundary layer on a non-catalytic wall is the simplest problem to treat, since no chemical reactions take place in the boundary layer or on the wall surface. However, the copper heat flux probe has a surface which is much closer to full catalycity than to no catalycity. Therefore, the case of a catalytic wall must be considered.

A catalytic wall imposes recombination of ions and atoms in the vicinity of the wall. Hence, in a frozen boundary layer on a catalytic wall, there is no chemistry source term in the flow, but there are chemical reactions near the wall and the species concentration varies across

the boundary layer, reaching a steady-state distribution in accordance to diffusion effects due to concentration gradients. In the equilibrium boundary layer case, the chemical composition is imposed by the temperature and pressure profile across the boundary layer. In that limiting solution, the wall catalycity does not play any role. Diffusion effects are negligible in the boundary layer but not near the wall, since diffusion of chemical energy adds to the heat flux just like in the case of the frozen boundary layer with catalytic wall. However, this effect can be taken into account by means of the equilibrium thermal conductivity. Under this hypothesis, one simply writes:

$$\vec{q} = - \lambda_{equ} \, \overrightarrow{grad} \, T \qquad (6.11)$$

At this point, we should note that there is not much difference in species concentration near the wall between an equilibrium boundary layer and a frozen boundary layer with a fully catalytic wall. The values of heat flux in both cases will then be almost identical [11]. The simplifying assumption of an equilibrium boundary layer then seems reasonable for the purpose of the calculation.

3.3.3 Governing equations

The governing equations of the axisymmetric, compressible equilibrium boundary layer equations are written as follows [12]:

$$\frac{\partial \, \rho u R}{\partial x} + \frac{\partial \, \rho v R}{\partial z} = 0 \qquad (12)$$

$$\rho u \frac{\partial u}{\partial x} + \rho v \frac{\partial u}{\partial z} = - \frac{\partial p_e}{\partial x} + \frac{\partial}{\partial z} \left(\mu \frac{\partial u}{\partial z} \right) \qquad (13)$$

$$\rho u \frac{\partial h}{\partial x} + \rho v \frac{\partial h}{\partial z} = u \frac{\partial p_e}{\partial x} + \mu \left(\frac{\partial u}{\partial z} \right)^2 + \frac{\partial}{\partial z} \left(\lambda_{eq} \frac{\partial T}{\partial z} \right) \qquad (14)$$

3.3.4 Change of variables

A combination of the Mangler transformation[4] and Howarth, Illingworth, Stewartson transformations[5] are used, in which the outer edge of the boundary layer is used as reference condition [13], unlike Fay and Riddell's choice of wall conditions. The Levy-Lees change of variables is given by [14]:

$$\xi (x) = \int_0^x \rho_e \, \mu_e \, u_e \, R^2 \, \mathrm{d}x' \qquad (15)$$

$$\eta (x, z) = \frac{R \, u_e}{\sqrt{2 \, \xi}} \int_0^z \rho \, \mathrm{d}z' \qquad (16)$$

---

[4] Transforming axisymmetric to equivalent 2D boundary layer equations.

[5] Transforming compressible to equivalent incompressible boundary layer equations.

and the new functions f, g and V are introduced such as:

$$f' = \frac{\partial f}{\partial \eta} = \frac{u}{u_e} \qquad (17)$$

$$g = \frac{T}{T_e} \qquad (18)$$

$$V = \frac{2 \, \xi}{\left(\frac{\partial \xi}{\partial x} \right)} \left(f' \frac{\partial \eta}{\partial x} + \frac{\rho v R}{\sqrt{2 \, \xi}} \right) \qquad (19)$$

It can be easily verified that all variables and functions are non-dimensional. The function V is introduced in order to reduce the order of the equations. If it was not done, terms proportional to the third derivative of f would appear in the equations.

3.3.5 Non-dimensional equations

Using the Levy-Lees transformation outlined above and performing the necessary substitution and algebra, the following equations are obtained for the stagnation-point solution:

$$\frac{\partial V}{\partial \eta} + f' = 0 \qquad (20)$$

$$V \frac{\partial f'}{\partial \eta} = \frac{1}{2} \left(\frac{\rho_e}{\rho} - (f')^2 \right) + \frac{\partial}{\partial \eta} \left(\chi \frac{\partial f'}{\partial \eta} \right) \qquad (21)$$

$$V \frac{\partial g}{\partial \eta} = \frac{1}{C} \frac{\partial}{\partial \eta} \left(\frac{\chi C}{Pr} \frac{\partial g}{\partial \eta} \right) - \frac{E}{C} \left[\frac{\rho_e f'}{2 \, \rho} - \chi \left(\frac{\partial f'}{\partial \eta} \right)^2 \right] \qquad (22)$$

The following non-dimensional symbols have been introduced, with c_p and λ taken as *equilibrium* values:

$$\chi = \frac{\rho \, \mu}{\rho_e \, \mu_e} \qquad (23)$$

$$C = \left(\frac{c_p}{c_{p,e}} \right) \qquad (24)$$

$$E = \frac{u^2}{c_{p,e} \, T_e} \qquad (25)$$

$$Pr = \frac{\mu \, c_p}{\lambda} \qquad (26)$$

The equations can be simplified to self-similar form (i.e. dependent on η only) because, by definition of the stagnation point, $\xi = 0$. This alone does not guarantee that all terms function of ξ vanish, however. In addition, the derivatives of u_e and T_e at the stagnation point can be shown to have the following limiting values:

$$\lim_{\xi \to 0} \left(\frac{2\,\xi}{u_e} \frac{\partial u_e}{\partial \xi} \right) = \frac{1}{2} \qquad (27)$$

$$\lim_{\xi \to 0} \left(\frac{2\,\xi}{T_e} \frac{\partial T_e}{\partial \xi} \right) = 0 \qquad (28)$$

3.3.6 Boundary conditions

The following boundary conditions for the transformed variables are used:

(wall, $\eta = 0$) $f' = 0$ (29)

(wall, $\eta = 0$) $g = \dfrac{T_w}{T_e}$ (30)

(outer edge, $\eta \to \infty$) $f' = 1$ (31)

(outer edge, $\eta \to \infty$) $g = 1$ (32)

3.3.7 Resolution scheme

The above system of equations is solved in a loosely coupled manner. Supposing that f' is given, the continuity equation (20) can be integrated in a straightforward way along the η co-ordinate. A uniform spacing has been chosen for the discretisation in η so that Simpson's rule can be used in the integration.

Supposing V known, the momentum (21) and energy (22) equations can then be solved. These equations are non-linear, but they can be cast in a general pseudo-linear form:

$$a\,y'' + b\,y' + c = 0 \qquad (33)$$

with, for the momentum equation ($y = f'$):

$$a = \chi \qquad (34)$$

$$b = \frac{\partial \chi}{\partial \eta} - V \qquad (35)$$

$$c = \frac{1}{2} \left(\frac{\rho_e}{\rho} - f'^{\,2} \right) \qquad (36)$$

and for the energy equation ($y = g$):

$$a = \chi / Pr \qquad (37)$$

$$b = \frac{1}{C} \frac{\partial}{\partial \eta} \left(\frac{\chi\,C}{Pr} \right) - V \qquad (38)$$

$$c = \frac{E}{C} \left(\frac{\rho_e f'}{2\,\rho} - \chi \left(\frac{\partial f'}{\partial \eta} \right)^2 \right) \qquad (39)$$

The coefficients a, b and c are function of f and g, but for the sake of solving the equations will be considered constants, computed using the results of the previous

iteration. The derivatives are replaced by 4th-order central finite differences[6] [15] and the value of the unknown functions are obtained at each discretised point along the η co-ordinate by solving the resulting linear system.

The solution method differs from what was outlined above for the sake of numerical efficiency [13]. The unknowns are actually replaced by 4th-order Lagrange polynomials of which the coefficients are computed so that the polynomial matches the exact solution of the differential equations in several arbitrary points [16].

3.3.8 Computation of heat flux rate

Based on the definition (11) of the heat flux rate and the transformation of the equations in non-dimensional space, the magnitude of the heat flux rate is simply given by:

$$q = \sqrt{\frac{2\,\beta}{\rho_e\,\mu_e}}\, T_e\,\rho_w\,\lambda_w\,g'_w \qquad (40)$$

The value of the derivative g'_w at the wall comes from the boundary layer computation. The outer edge parameters come in the picture from the Levy-Lees transformation.

3.3.9 Stagnation-point velocity gradient

For the typical geometry of the ESA sample holder, idealised by a cylinder of radius R_m with a flat face placed perpendicularly to the flow, it is not possible to obtain an expression for the velocity gradient based on theory alone. Kolesnikov [17] proposed the following relation, based on computations and experimental observations:

$$\frac{\beta\,R_m}{U_e} = \frac{1}{2 - \zeta - 1.68\,(\zeta-1)^2 - 1.28\,(\zeta-1)^3} \quad (\zeta \le 1) \quad (41)$$

$$\frac{\beta\,R_m}{U_e} = \zeta \qquad (\zeta > 1) \quad (42)$$

with $\zeta = R_m / R_j$, R_j being the plasma jet radius.

For other, simpler geometries, like the cylinder or sphere, potential flow results can be used to provide a reasonably accurate value of the stagnation-point velocity-gradient in inviscid flow.

---

[6] Forward and backwards 4th-order finite differences are used on the sides of the discretised space, where a central formula cannot be applied.

3.4 Relating flow properties to experimental measurements

3.4.1 Principle of the method

Let us suppose that the models described above are available to compute the stagnation-point heat flux rate q and the stagnation pressure on the Pitot tube p_{Pitot}. The flow properties in which we are interested are the pressure p, density ρ, temperature T and velocity u, from which all other flow properties can be computed. Since the measurements are performed in a subsonic plasma jet, the static pressure in the jet is constant and equal to the test chamber pressure. Then, only temperature is required before the chemical composition can be computed. The computation of the heat flux rate requires a knowledge of the equivalent outer flow values on the probe, i.e. the total pressure and temperature, to serve as boundary conditions:

$$q = q\ (p_t,\ T_t,\ u) \qquad (43)$$

If the full exact solution of the boundary layer equations cannot be implemented or for first analysis, the stagnation-point heat transfer formula of Fay and Riddell for the equilibrium boundary layer [11] can be used. It yields a heat flux accurate within 10%:

$$q = 0.76\ Pr_w^{-0.6}\ (\rho_e\ \mu_e)^{0.4}\ (\rho_w\ \mu_w)^{0.1}\ \sqrt{\beta}\ (H_t - h_w)$$

$$\times \left(1 + (Le - 1)\ \frac{h_D}{H_t - h_w}\right)^{0.48} \qquad (44)$$

3.4.2 Set of equations without correction for the Barker effect

In this case, the Pitot probe is supposed to exactly measure the total pressure of the flow. The probe measurements thus provide values of total pressure $p_t{}^{\circ}$ and heat flux q°. The static pressure p° in the chamber is known. Then, the following system of three equations can be written, expressed in three unknowns T_t, T and u which yield the aerothermodynamic state of the gas ahead of the probe:

$$\begin{cases} q\ (p_t{}^{\circ},\ T_t,\ u) - q^{\circ} = 0 \\ H_t\ (p_t{}^{\circ},\ T_t) - [h\ (p^{\circ},\ T) + 0.5\ u^2] = 0 \\ S_t\ (p_t{}^{\circ},\ T_t) - s\ (p^{\circ},\ T) = 0 \end{cases} \qquad (45)$$

This system can be solved using a Newton-Raphson iterative procedure.

3.4.3 Set of equations with correction for the Barker effect

The above system supposes that the total and stagnation pressures are equivalent, a hypothesis which is probably hardly verified in practice. If the low-Reynolds correction to Pitot pressure (known as the "Barker effect") has to be included, then the total pressure becomes an

additional unknown [18]. Hence, (45) must be transformed into a system with four unknowns by way of the total pressure correction defined in terms of a coefficient C_p, function of the Reynolds number, which is itself a function of pressure, temperature and velocity:

$$\begin{cases} q\ (p_t,\ T_t,\ u) - q^{\circ} = 0 \\ H_t\ (p_t,\ T_t) - [h\ (p^{\circ},\ T) + 0.5\ u^2] = 0 \\ S_t\ (p_t,\ T_t) - s\ (p^{\circ},\ T) = 0 \\ p_{Pitot} - p^{\circ}_{Pitot} = 0 \end{cases} \qquad (46)$$

with

$$p_{Pitot} = p_t + 0.5\ \rho\ (p^{\circ},\ T)\ u^2\ [C_p\ (p^{\circ},\ T,\ u) - 1] \qquad (47)$$

The final system, solved using the Newton-Raphson procedure, is written out as follows, with the elements of the Jacobian matrix computed, as usual, using numerical finite differences[7]:

$$\begin{pmatrix} 0 & \dfrac{\partial q}{\partial u} & \dfrac{\partial q}{\partial T_t} & \dfrac{\partial q}{\partial p_t} \\ -\dfrac{\partial h}{\partial T} & -u & \dfrac{\partial H}{\partial T_t} & \dfrac{\partial H}{\partial p_t} \\ -\dfrac{\partial s}{\partial T} & 0 & \dfrac{\partial S}{\partial T_t} & \dfrac{\partial S}{\partial p_t} \\ \dfrac{\partial p_{Pitot}}{\partial T} & \dfrac{\partial p_{Pitot}}{\partial u} & 0 & \dfrac{\partial p_{Pitot}}{\partial p_t} \end{pmatrix} \begin{pmatrix} \Delta T \\ \Delta u_t \\ \Delta T_t \\ \Delta p_t \end{pmatrix}$$

$$= \begin{pmatrix} q^{\circ} - q\ (p_t,\ T_t,\ u) \\ [h\ (p^{\circ},\ T) + 0.5\ u^2] - H_t\ (p_t,\ T_t) \\ s\ (p^{\circ},\ T) - S_t\ (p_t,\ T_t) \\ p^{\circ}_{Pitot} - p_{Pitot} \end{pmatrix} \qquad (48)$$

The iterative process is continued until the residuals (right-hand side vector) have reached a sufficiently low value (in our case, 10^{-9}, usually reached in 10 to 20 iterations – a few cases were tougher to compute, not converging beyond 5 orders of magnitude).

3.5 Facility and data reduction charts

The development of the data reduction model using the stagnation-point heat transfer and Pitot probe models allows us to numerically build *performance maps*, i.e. charts that relate the Plasmatron parameters and the flow stagnation properties. Since three boundary conditions are needed to completely determine the conditions of each run, it is impossible to represent the facility performance on a single diagram. One possible choice, which comes naturally, is to freeze the test

---

[7] There are no practical closed-form explicit analytical expressions for these derivatives, due to the chemistry.

chamber pressure and to represent the facility performance as a function of the two remaining parameters, mass flow rate and power. The sample geometry and temperature must also be defined for the heat flux computation. The heat flux probe geometry (figure 15) has been used with a wall temperature of 400 K. This is about 50 K lower than the boiling point of water at 10 bars, the maximal temperature that the cooling water can reach in the probe. The low values of heat flux are then underestimated because the probe will actually be colder.

Figure 21 (a to e) shows the performance maps at pressures of 15, 25, 75, 125 (the four pressure levels used in the tests) and 175 hPa respectively. The maps are drawn with Mach number and flow temperature as axes. Each figure comes with two maps: the one on the right is used to determine the operating conditions (Mach number and temperature) from the testing conditions (stagnation point heat flux and total pressure). The other on the left is used to determine the values of equivalent mass flow rate (tilted right) and power (tilted left) of the flow.

It should be noted that the power and mass flow rate indicated by the charts above do not correspond to the facility settings, but are computed based on constant flow properties across the jet, as in a quasi-one-dimensional model. The difference is shown on figure22, where it is readily seen that the mean value of any real flow property is lower than the equivalent quasi-one-dimensional value taken for that property.
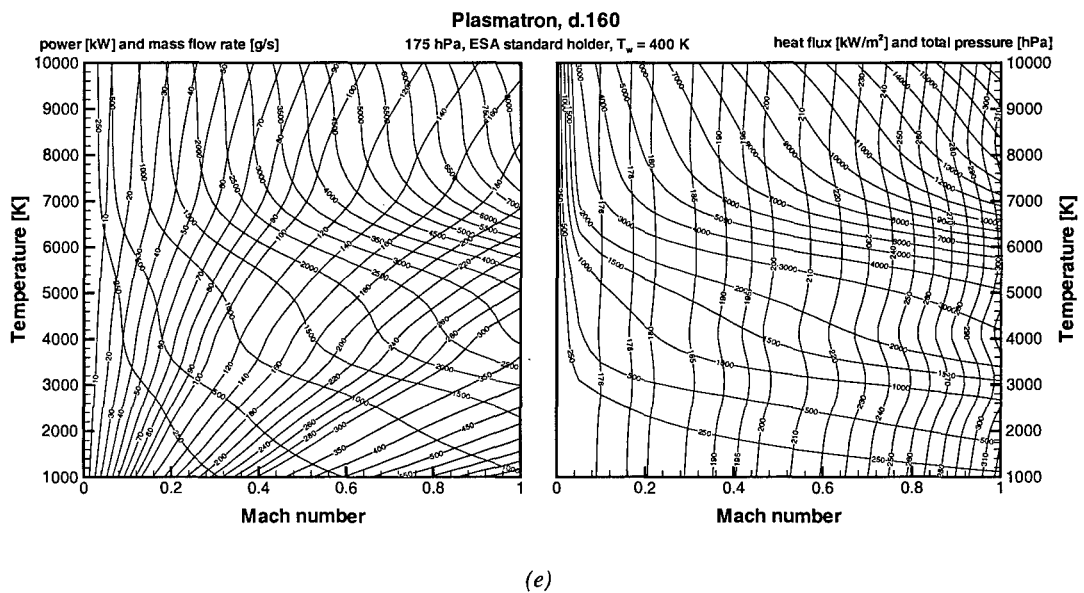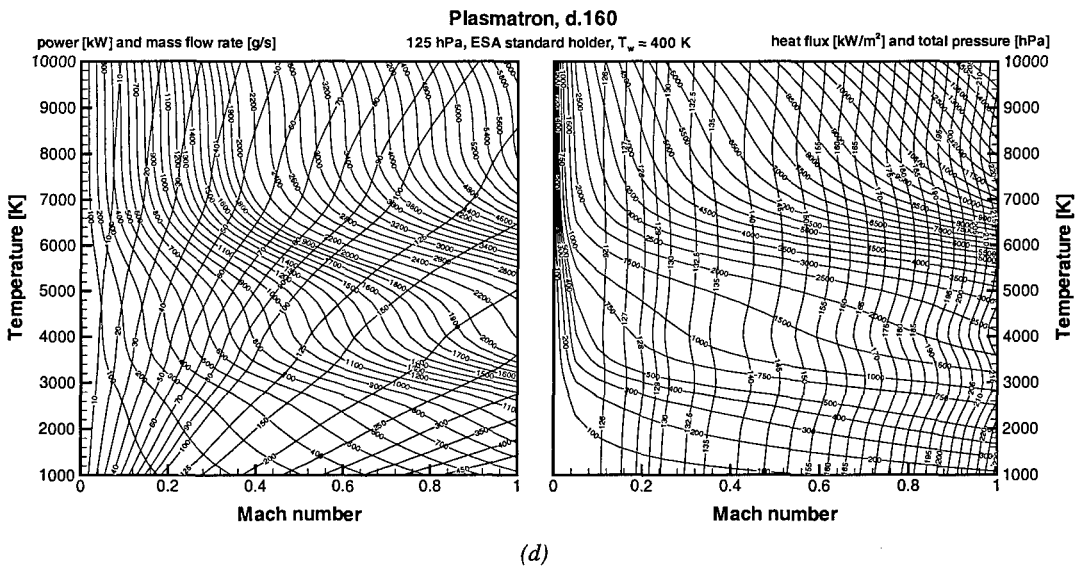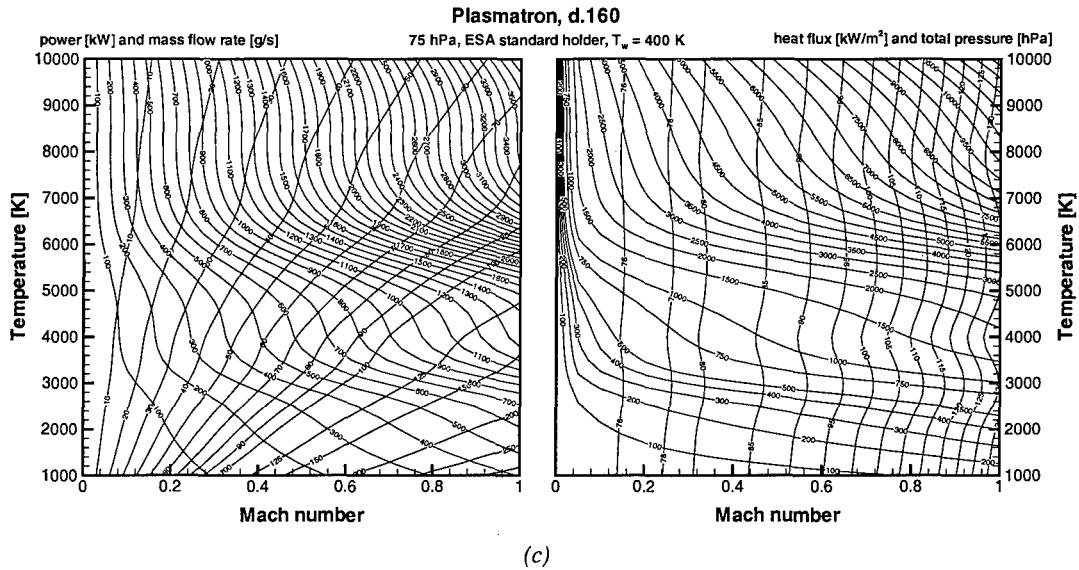

(a)

(b)
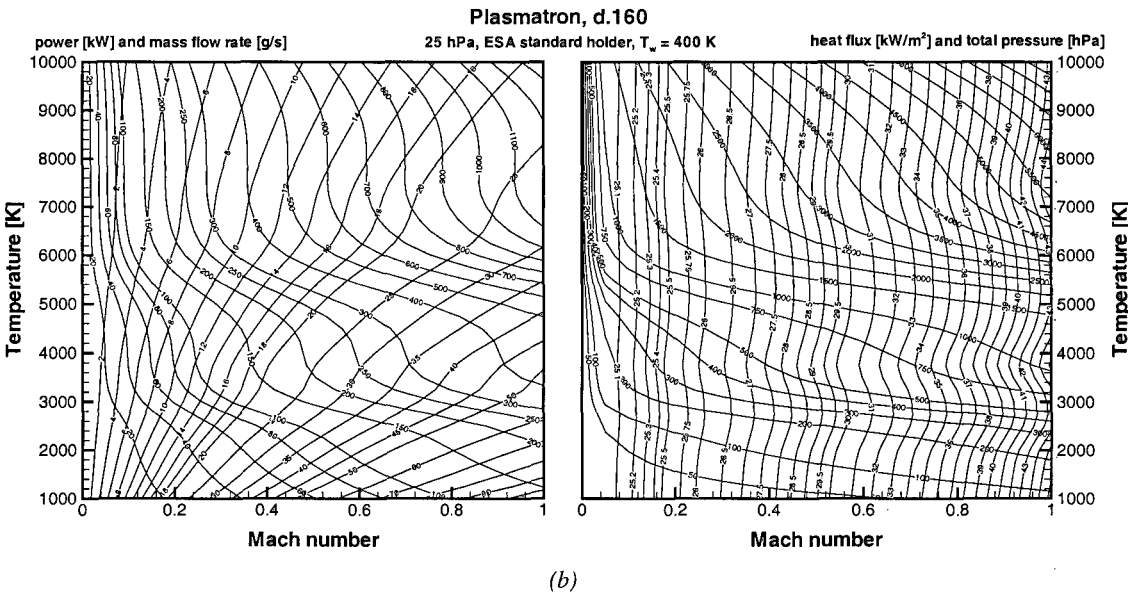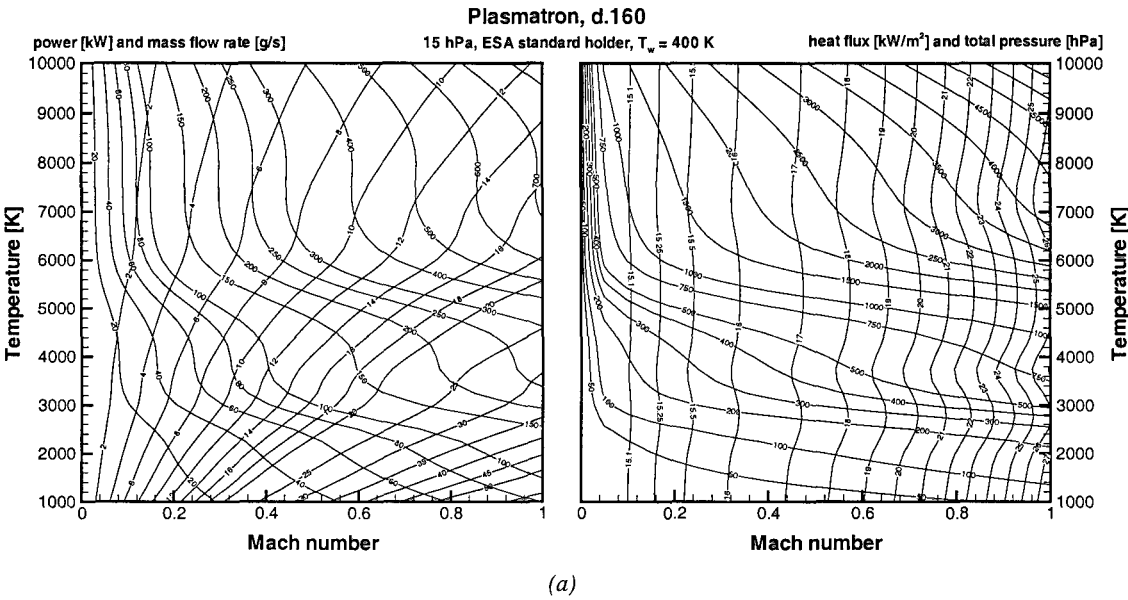
Figure 21. Plasmatron performance maps at various chamber pressures – 160 mm diameter torch.
(a) 15 hPa – (b) 25 hPa – (c) 75 hPa – (d) 125 hPa – (e) 175 hPa
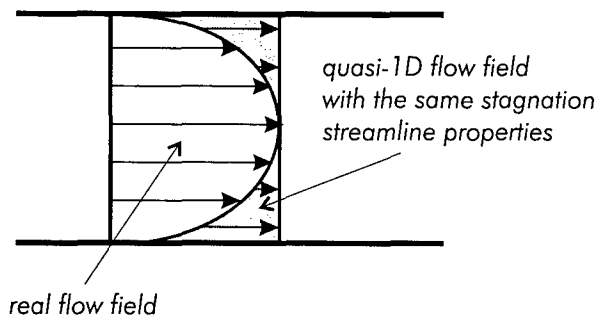
6-16

Figure 22. Difference between the real field and the quasi-1D flow field used in the performance maps

Detailed calibration of the facility is required to be able to relate the two values one to another. We have shown [18] that it was generally not possible to do so in the Plasmatron facility because the equivalent value for the mass flow rate does not vary according to a simple function of the mean mass flow passing through the facility. However, the charts presented above can still be used to obtain, at a glance, the values of temperature and Mach number on the measurement streamline from the measured values given by the probes.

4. Facility performance

4.1 Performance tests versus the heat flux versus static pressure diagram

4.1.1 Introduction

Global performance measurements were carried out in the scope of the preliminary calibration, as a verification of the compliance of the facility to ESA requirements (as outlined on figure 3. During that first phase, heat flux measurements were carried out at different axial positions with many different facility settings.

4.1.2 Axial position of the probes

The test conditions considered in the present work are defined as follows. The Plasmatron SMIM[8] allows only a limited number of measurement positions in the test section. Table 3 shows the nomenclature associated with each position and the distance between the torch exit and the tip of the probe. The heat flux probe or the Pitot probe can be mounted on the SMIM, but only one probe can be used at the same time.

---

[8] *Side Model Injection Mechanism*, a temporary probe support system that can be fixed on the side portholes. It will be replaced in the future by the MITM, *Model Injection and traversing Mechanism*.

designation	distance (mm)
AA1	39
AA2	139
AA3	(189)
AC1	193
AC2	293
AC3	(343)
AR1	347
AR2	447
AR3	(497)

Table 3. SMIM probe positions at the first porthole (distances between parentheses require additional equipment not manufactured at the time of writing)

The first measurements were carried out from the second porthole, at 1100 mm from the torch, as a precaution against overheating. Measurements were then taken at more forward positions from the first porthole. Four positions were considered in this work: AR2, AR1, AC1 and AA1 (as defined in table 3). Given the results of the heat flux measurements at AC1, it was decided that testing in the AA1 position, closest to the torch, could not safely be conducted with the present heat flux probe design, and positions closer than AC1 were dropped out of the study.

4.1.3 Facility settings

Facility settings used to control the test conditions are generator power, gas mass flow rate and chamber static pressure. For the first series of test, which involved illustrating the performances, a wide combination of the parameters were used. In second and more detailed calibration phase, only 4 pressure levels were considered: 15, 25, 75 and 125 hPa. Power levels were chosen to be 150, 250 and 300 kW, mass flow rate levels 8 and 16 g/s. All their combinations lie in the domain of stability of the 160 mm diameter plasma torch and are easily related one to another by simple ratios, except the condition at 8 g/s and 300 kW, which is out of the domain at low pressure and has therefore not been tested.

4.1.4 Results of the first heat flux measurements

The first series of heat flux measurements are summarised on figure 23 in function of static pressure. As it is seen, the original requirements are largely exceeded, as indicated by the high heat flux rates observed in all the pressure range, up to 2.8 MW/m^2. This is beneficial to the future use of the facility: not only does it give more flexibility in testing capabilities, but it also ensures that reasonable tests can be carried out on many different re-entry configurations. Indeed, the heat flux measured here are recorded on a fully catalytic surface. Real TPS samples are subject to lower heat fluxes for the same value of stagnation enthalpy. Therefore, they require a testing environment with more

enthalpy for the same value of heat flux. The peak heat flux of 2.8 MW/m^2 has been measured at a power setting of 250 kW and at 193 mm from the torch exit. Extrapolating the value to the torch exit, one finds that the peak heat flux close to the torch might be of 3500 kW/m^2. Taking into account the power still available, still higher heat fluxes are conceivable.
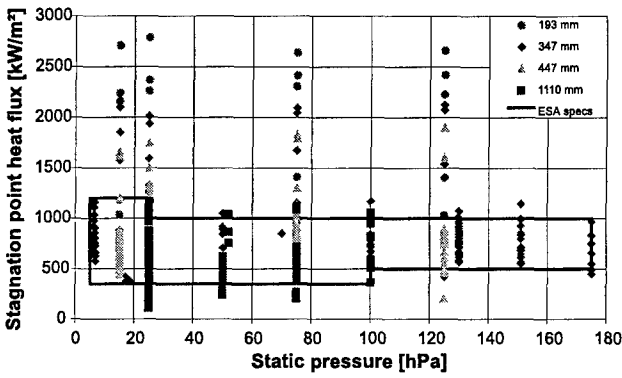

Figure 23. Heat flux performance of the Plasmatron compared to the original ESA requirements

4.2 Use of Pitot and heat flux traverses as a validation tool

4.2.1 Introduction

Although the Pitot and heat flux probes have been designed primarily to record the contractual performance of the facility, they can be used to obtain other data as well. We have performed traverses of Pitot and heat flux across the jet, in order to obtain radial profiles of dynamic pressure and heat flux. Figures 24a and b show photographs of the probes in the 160 mm diameter jet. The pictures clearly show that the blockage of the Pitot probe is relatively small but that the blockage of the heat flux probe is quite important. Therefore, heat flux probe traverses are used only to obtain an order of magnitude confirmation of the jet enthalpy. They cannot yield extremely accurate measurements.
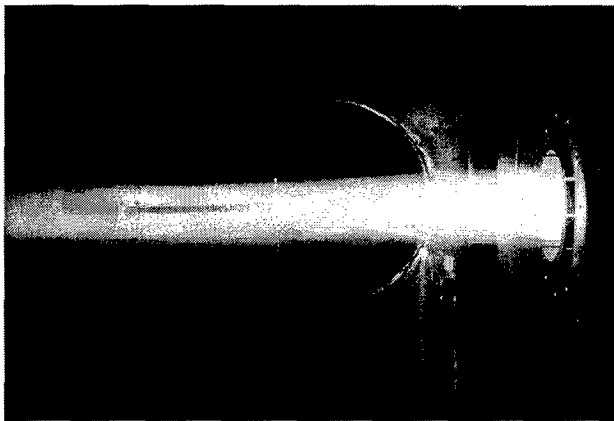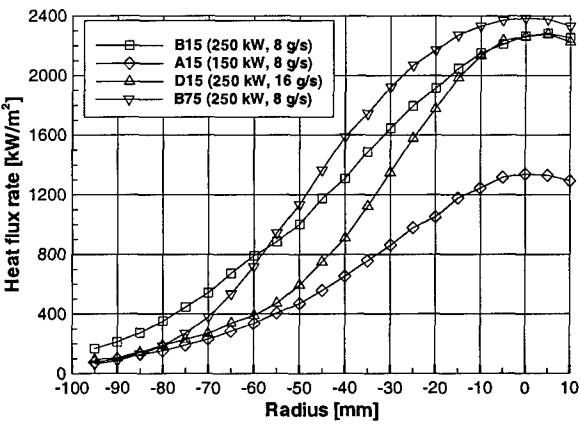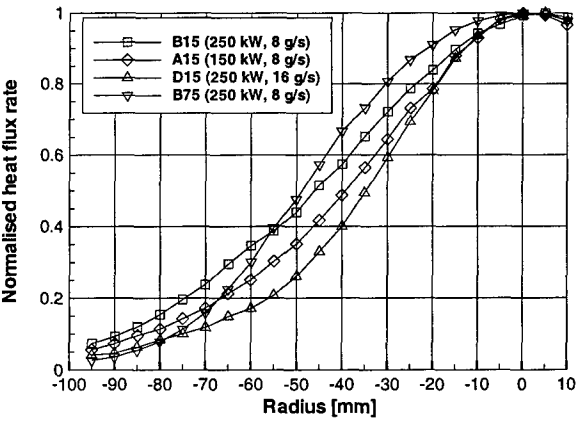

(a) Pitot probe
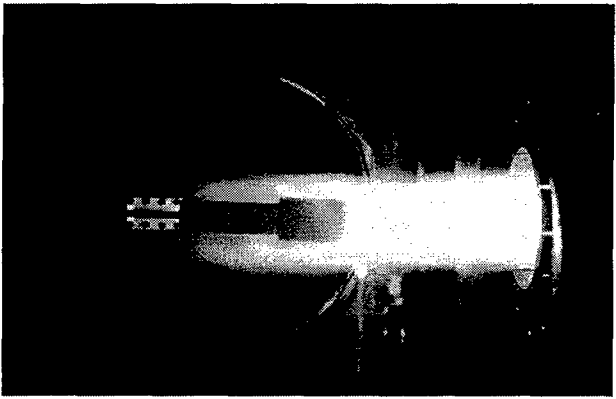
(b) Heat flux probe

Figure 24. Pitot and heat flux probes in the plasma jet

(a) measured traverses

(b) non-dimensional traverses

Figure 25. Heat flux traverses across the plasma jet at position AC1 (193 mm)

4.2.2 Analysis of the traverses regarding two-dimensional flow characteristics

Only four traverses were made in order to observe the effect of each parameter. The reference condition was chosen as B15 (8 g/s, 250 kW, 15 hPa). From there, the three other conditions were obtained by doubling

the mass flow (D15), using 150 kW power (A15) and increasing the pressure to 75 hPa (B75). All traverses have been done at 193 mm from the torch exit. Figure 25 shows the results of the heat flux probe traverses, in dimensional (a) and non-dimensional (b) form. In the latter case, the values have all been divided by the corresponding centreline value. Figure 26 shows the same type of plot for the measured Pitot pressure, i.e. the difference between Pitot and static pressure.

The heat flux traverses confirm the linear dependence of heat flux on power: the A15 peak value has about 0.6 times the value of the B15 peak, and the non-dimensional heat flux curves of A15 and B15, although not superimposed, are closest one to another. The same trend is found for the Pitot reading. This can be understood by expressing the Pitot reading in function of the Mach number (assuming here incompressible flow):

$$p_{Pitot} - p = \frac{\gamma}{2} p \, M^2 \qquad (49)$$

As total enthalpy increases linearly, so temperature does, and therefore so does M^2.
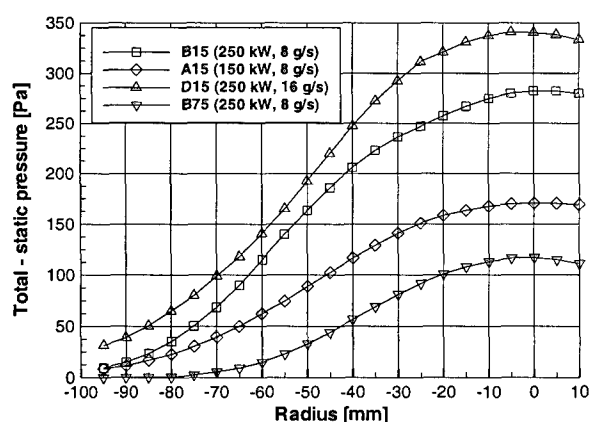
(a) dimensional traverses
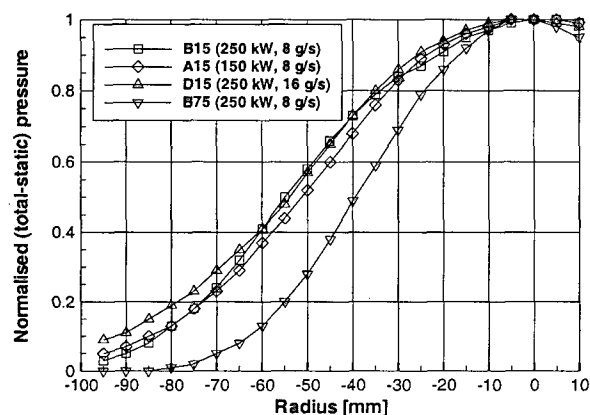
(b) non-dimensional traverses

Figure 26. Traverses of Pitot measurements across the plasma jet at position AC1 (193 mm)

The effect of increasing pressure creates a more full heat flux profile and a more empty Pitot profile. Increasing the pressure increases the density, therefore at constant mass flow and power the velocity drops accordingly. The jet is also smaller, which partly explains why this profile is not similar to the others.

The effect of doubling the mass flow rate does not even double the Pitot pressure, and more surprisingly it does not affect the heat flux rate on the centreline. A probable explanation for this closeness of the results at 8 and 16 g/s can be drafted as follows: when the mass flow increases at constant power, the total enthalpy should decrease accordingly. However, the inductive heating still requires a high temperature close to the torch centreline, in the coupling region. The relative constancy of total enthalpy on the centreline can therefore be a direct result of this constant high temperature in the torch. Since less total enthalpy is globally available, the heat flux must be lower on the edges if energy is to be conserved

4.2.3 Corrections applied to the traverse measurements

The traverses can be processed using the same technique as the one used to process the centreline measurements. This allows to obtain computed traverses of temperature, velocity and total enthalpy. The integration on the jet section of the mass flow and power should yield values close to the mass flow and power used in the torch.

The process is not of extreme quantitative pre- cision, however. If a traverse made in a 160 mm diameter jet by a 12 mm diameter Pitot can still be thought of as reasonable, it is certainly not the case of the heat flux traverses. As said before, the blockage of the probe (50 mm diameter) is such that the displacement effect and the change in stagnation-point velocity gradient become considerable.
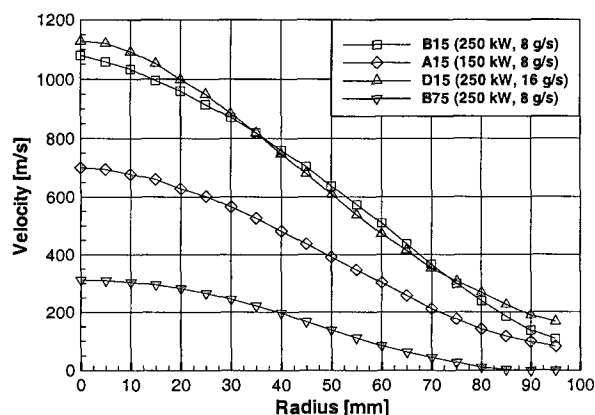

Figure 27. Computed velocity traverses at position AC1 (193 mm)

Figure 27 shows the computed velocity traverses and figure 28 the total enthalpy traverses. The latter clearly shows an artefact effect from the size of the heat flux probe: as the heat flux does not go sufficiently down close to the edge of the jet, the total enthalpy is overestimated, even more so as velocity drops down.
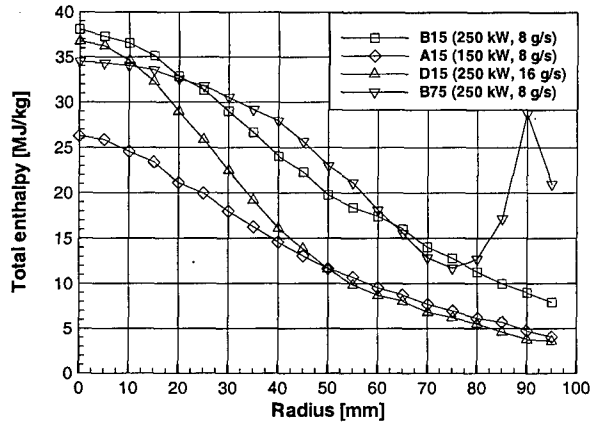

Figure 28. Computed total enthalpy traverses at position AC1 (193 mm)

The velocity results show that the traverse has not been carried out to the edge of the jet, as a residual velocity is measured, in some cases of hundreds of meters per second. This could be due to the fact that the jet has opened beyond or to the fact that the high heat flux on the edge automatically gives a significant velocity. Both explanations are equally valid, as figure 26a shows a significant dynamic pressure at the edge in some cases.

The traversing mechanism does not allow to explore radial positions below −95 mm. Hence, a possible correction scheme is to smoothly extrapolate the readings to a reasonable jet edge. Based on a fair extrapolation of the curves, the traverses were extended to −110 mm in the 8 g/s case and −120 mm in the 16 g/s case (see figure 29a for heat flux and b for dynamic pressure).

It is also necessary to apply a displacement effect correction to the measurements, which takes into account the fact that the flow upstream of either probe is non-uniform. The gradient of incoming velocity in the flow has two effects: (1) because the dynamic pressure is proportional to the square of the velocity, its integration over the orifice or sensor does not yield the same value as the exact value in the geometrical centre (this *velocity head correction* is usually negligible with respect to the other effect); (2) the streamlines in front of the Pitot probe and, to a greater extent, in front of the heat flux probe, are deflected towards the region of low velocity, causing the probe to record a higher stagnation pressure or heat flux than the one existing at the probe location. This second effect has been theoretically studied by Lighthill, who proposes the following correction for a Pitot probe [19]:

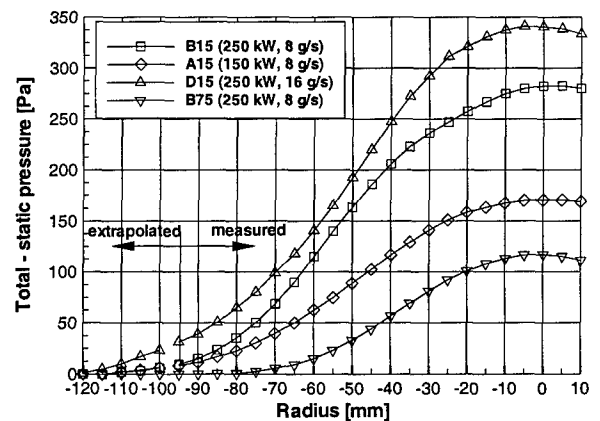$$\frac{\delta}{D} = 0.45\,a - 1.35\,a^3 \tag{50}$$

with δ the correction to the radial position of the measurement (towards the centre of the jet), D the probe diameter and a a parameter based on the gradient of velocity in the jet, defined as:

$$a = \frac{\Delta u}{\bar{u}} \tag{51}$$

with $\bar{u}$ the mean velocity of the gradient Δu. This expression was used to correct both Pitot and heat flux measurements.
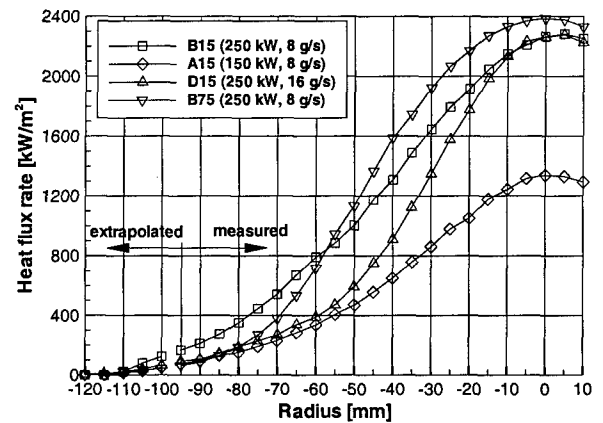
(a) heat flux probe reading

(b) Pitot probe reading

Figure 29. Extrapolated traverses of Pitot pressure and heat flux rate

4.2.4 Integration of the traverses and comparison with facility settings

It is possible to integrate the computed traverses of density, velocity and total enthalpy in order to compute the mass flow rate and the plasma power in the jet, according to:

$$\dot{m} = 2 \pi \int_0^R \rho\,(r)\; u\,(r)\; r\,\mathrm{d}r \qquad (52)$$

$$P = 2 \pi \int_0^R \rho\,(r)\; u\,(r)\; H_t(r)\; r\,\mathrm{d}r \qquad (53)$$

If these values have to be compared to the mass flow rate and power settings of the facility, the correction for jet entrainment must also be taken into account. The values of mass flow have been corrected using following formula, derived by Schlichting [20] for laminar entrainment, using a mean value of viscosity:

$$\frac{\partial \dot{m}}{\partial x} = 8 \pi \mu \qquad (54)$$

The entrained mass flow rate is subtracted from the measured mass flow rate to obtain the final corrected mass flow rate. The entrained power is also subtracted from the measured power, although the contribution in this case is quite small as the surrounding air is supposedly cold.

Results of the integration of mass flow and power with and without taking into account the corrections are summarised in table 4. The displacement effect causes a shift of up to 4.7 mm (heat flux probe) and 1.2 mm (Pitot probe) on the edge of the jet. The entrainment mass flow rate is of the order of 0.6 g/s in all cases.

Table 4 indicates that the global mass flow is accurately computed in the 8 g/s case, and less so in the 16 g/s case. However, the jet was rather arbitrarily extended to 120 mm radius; if it is extended to 115 mm, the corrected mass flow is then 15.49 g/s (−3.2 %), which yields a much better agreement. It seems reasonable to conclude, from this example, that integration of the traverses yield mass flow values close to those used in the facility.

	facility		uncorrected			
	$\dot{m}$ [g/s]	P [kW]	$\dot{m}$ [g/s]	error [%]	P [kW]	error [%]
A15	8	90	7.81	−2.37	87.61	−2.60
B15	8	150	8.63	7.87	167.90	11.93
D15	16	150	13.39	−16.31	147.06	−1.96
B75	8	150	6.78	−15.25	167.57	11.71

	facility		corrected			
	$\dot{m}$ [g/s]	P [kW]	$\dot{m}$ [g/s]	error [%]	P [kW]	error [%]
A15	8	90	7.89	−1.41	82.48	−8.35
B15	8	150	8.04	0.51	156.84	4.56
D15	16	150	17.1	6.90	145.58	−2.94
B75	8	150	7.93	−0.83	164.75	9.83

Table 4. Results of the integration of mass flow and power using the computed traverses

The values of power are in slightly worse agreement, although they all lie within the experimental uncertainty of the heat flux probe measurements. These results seem to indicate that the methodology used here is valid. It also means that the flow is not far from chemical equilibrium or that chemical non-equilibrium does not play a significant role on total pressure and stagnation-point heat flux.

The comparison above can be performed on any facility and should be one of the first tests to be performed in order to assess the overall quality of the developed measurement techniques. However, it can be carried out only if some knowledge of the efficiency is available. Indeed, the power settings is applied to the power generator, which is different from the power in the plasma jet due to numerous losses. If the facility cooling system is properly instrumented, an indicative value of the efficiency can be deduced from the conservation of power. In the case of the Plasmatron facility, we obtained a global efficiency of about 60% [6].

5. measurement techniques in development

5.1 Introduction

5.1.1 The VKI Minitorch

The VKI inductively coupled plasma "Minitorch" was first ignited in December 1996. It is a small facility, operating at gas flow rates of the order of 1 g/s, and using a 30 mm diameter plasma torch, supplied by a high frequency (27.12 MHz) vacuum triode oscillator which delivers up to 15 kW anode power at anode voltage up to 6 kV (figure 30).

The Minitorch was designed as a pilot facility during the design and construction at VKI of the bigger and more powerful 1.2 MW Plasmatron. Changes in torch geometry and operating conditions can very easily be made to study the effect of the various torch parameters and gain experience in ICP torch operation. This plasma facility is also used as a test bench to test and validate the measurement techniques and methods, before their implementation on the plasmatron.

5.1.2 Measurement developments

The latest measurement technique implemented in the Minitorch is the Laser Doppler Velocimetry (LDV). This technique is non-intrusive and provides accurate detailed measurements of the flow field of the plasma jet. It is not the aim of this note to present in details the principles of the LDV technique, but to show its

adaptation for plasma flow characterisation. Briefly, it consists in measuring the plasma flow velocity by recording the scattered signal of a seeding particle passing trough the interference region of two coherent laser beams (figure 31).
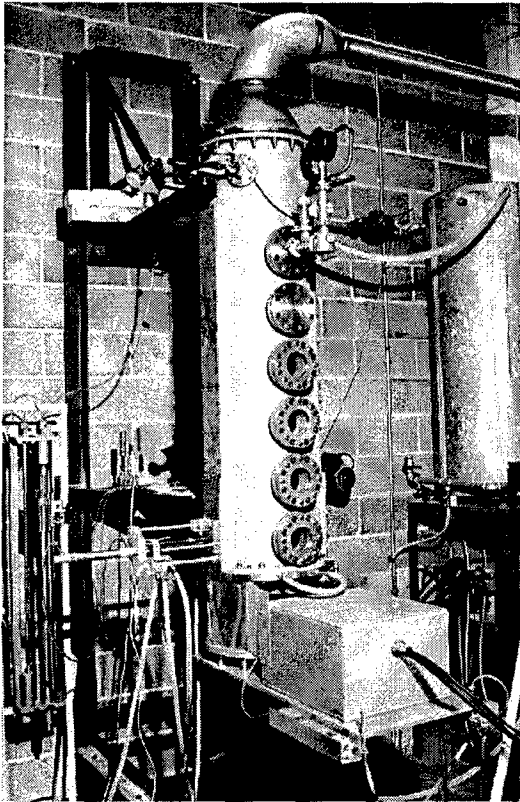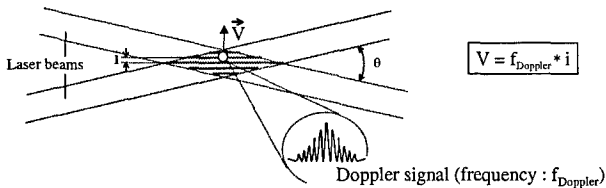

Figure 32. Classical LDV set-up

5.2.2 Optics

The plasma discharge is a very bright source which emits on a large wavelength spectrum. One has to check if the wavelengths of the laser beam used for the measurement are not corresponding with a peak of the plasma spectrum. When working with an air plasma, we can avoid overlaps of the LDV signal by using an argon laser (figure 33). Nevertheless one has to use an interference filter because the plasma is an intense source of light and leads to a saturation of the photo-multiplier.

Figure 30. The minitorch facility
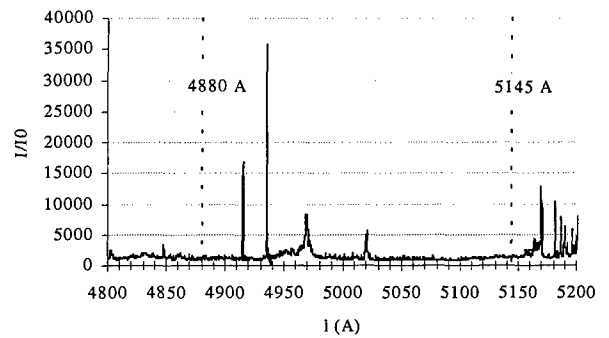
Figure 33. Air plasma wavelength spectrum
$(4800 < \lambda < 5200 \text{ Å})$

Figure 31. Basic principles of LDV measurements

The filter allows to reduce the perturbation due to the thermal emission of the particle heated in the high enthalpy flow which can lead to noisy signals. Another problem concerns the presence of temperature gradients which can introduce variations of the refraction index and disturb the interference pattern in the probing volume. From experiments with Schlieren photography in plasma jets at low pressure [21] and from literature about LDV measurements in hot gases [22], one can consider this effect as negligible in general cases. On the other hand one has to worry about the optical accessibility of the plasma flow to realise a good optical alignment.

5.2 LDV measurements

5.2.1 Introduction

The classical set-up for LDV measurements, which is used with forward scattering, is shown in figure 32. It contains a laser, a beam splitter, lenses, filter, photo-multiplier, particle generator and an electronic device. In a severe environment like a plasma flow, preliminary studies on the optical device used and on the behaviour of the chosen particles are needed in order to define good conditions for such measurements.
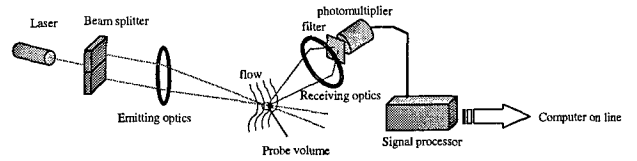
5.2.3 Seeding

The seeding conditions in plasma flows are one of the worst that can be encountered as they consist in a gas at high temperature under low pressure. The particle generator must allow to work in such conditions. Previous experiments in combustion [23] and in argon plasma [24] can guide us to choose a convenient

apparatus. The solid particles are the most adapted ones, but their polydisperse nature appears to be a problem. Filters or special selection in or before the particle generator are usually needed. The cyclone aerosol generator seems to be a good candidate since it is a simple device. It has already been used successfully for Al_2O_3 particles to seed flames [25]. Other more sophisticated particle generators can be used for specific applications [23]. It has to be noticed that seeding problems can appear before reaching the plasma discharge. Actually, during the process of particle transport in pipes, the seeding can decrease drastically because of particle deposition on the tube wall. The powder has to be in good condition to be injected in the flow. Possible electrostatic charge or humidity have to be removed.

5.2.4 Particles behaviour

It is out of the scope of this report to study in detail the behaviour of particles in a high enthalpy flow. We just want to indicate the relevant parameters that have to be checked to be in good conditions for LDV measurements. The particles are exposed to a low-density fluid with high temperature. They have to be small enough to follow the fluid, but big enough to resist to the strong heat transfer at which they are exposed. The motion of the particles and their thermal resistance have to be inspected.

The ability of a particle to follow the flow depends on its shape, size, relative density with respect to the density of the fluid and particle concentration. An easy way of characterising particle dynamics effects is to examine the Stokes number:

$$St = \frac{\tau_p}{\tau_f} \qquad (55)$$

where τ_p is the characteristic particle response time and τ_f is the time scale of the flow variations. For $St \ll 1$, the particles will effectively follow the fluid motions to be measured. τ_f is evaluated as the diameter of the torch over the mean velocity of the flow for the working condition of the torch. The particle time τ_p is defined by [26]:

$$\tau_p = \frac{\rho_p d_p^2}{18 \mu} \qquad (56)$$

In order to check the particles ability to support the heating from the plasma flow during their flight we have to estimate their total evaporation time. The complete solution of the evaporation of a material in a plasma discharge has been already examined [27]. This unsteady problem is not trivial and takes into account many effects of heat and mass transfer phenomena. A rough calculation of this consumption time τ_c can be considered assuming a pure heat transfer conduction to the particle [21]. A non-dimensional life duration number can be defined as the ratio between the consumption time and the time of flight of the particle in the discharge (τ_r):

$$L_d = \frac{\tau_c}{\tau_r} \qquad (57)$$

Others authors take into account a "heating number" S_p to select the particle to be used. It represents the ratio between the heat which is contained per unit volume of the particle at its melting point and its density [28]. From the literature, alumina (Al_2O_3), zirconium oxide (ZrO_2) and porous zirconium oxide (ZrO_2') appear to be adapted for LDV measurements in high enthalpy flows [28], [29]. ZrO_2' presents the advantage to be lighter with a good thermal resistance. As an example, the Stokes number and life duration number for Al_2O_3, ZrO_2 and ZrO_2' are calculated for typical plasma conditions ($T = 6000$ K, $\dot{m} = 0.5$ g/s) on figures 34 and 35.
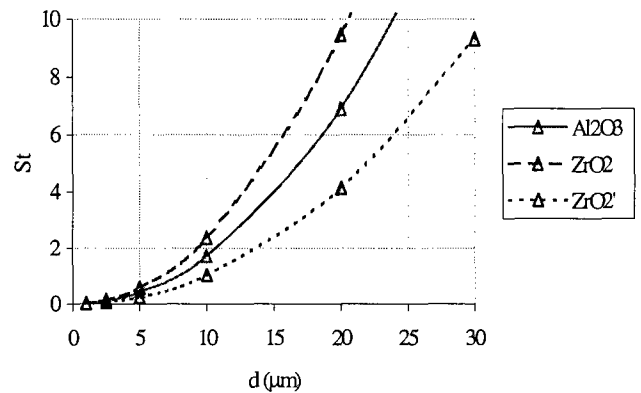
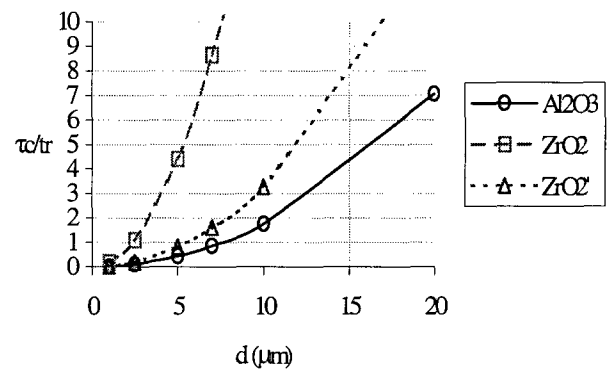Figure 34. Stokes number of particles in a plasma flow

Figure 35. Non-dimensional life duration of a particle in a plasma flow

A remark has to be done for seeding realised with metallic powders. When the static pressure increases in the test chamber, the time residence of the powder become larger and the evaporation rate increases. The presence of the metallic vapour in the coil region significantly changes the electrical properties of the discharge. This change of impedance leads to electrical instabilities and it becomes difficult to control the power transferred to the plasma charge. Moreover, we

have to mention that thermophoresis forces can be notable because of temperature gradient [24].

5.2.5 Signal processing

Once the optical adjustment and a good seeding have been achieved, the signal from the particle scattering must be processed to get the flow velocity. This signal is then firstly collected in a pinhole through an objective and guided by an optic fibre to a photo-multiplier. The electrical signal is filtered and analysed in the signal processor device. Its role is to select the valid signal which contains relevant information to deduce the flow velocity. The main parameter to measure is the signal frequency ($f_{Doppler}$) since the particle velocity (V) is given by:

$$V = f_{Doppler} \ i \tag{58}$$

where i is the fringe spacing.

In many cases the signal to measure, usually called "Doppler burst", can easily be affected by several sources of disturbances. A faraday cage has to be placed around the ICP torch to limit its electromagnetic radiation to the surroundings. The alteration of the signal can also be caused by a slight misalignment in the laser beam cross section or by a bad intensity balance between the beams. These problems can be checked by the operator. The disturbance coming from the particles are more difficult to control. Actually the dispersion in particle diameter can lead to big differences in light scattering. The thermal emission of the particles, heated in the high enthalpy flow, can induce noisy signals. Moreover the particles which cross the control volume partially or in a bad way have to be removed in order to process a correct value for the velocity. Since we measure relatively high velocities, few light is scattered and the voltage of the photomultiplier has to be increased. This amplifies the noise level as well. Figure 36 shows typical non-filtered and filtered signals from SiO_2 particles in the plasma jet of the Minitorch facility.

5.2.6 Experiments

The measurements have been done for two static pressures in the test chamber and two average total enthalpies of the jet. This represents four working conditions for the ICP torch reported in table 5. Let us remember that the average total enthalpy is defined by the ratio between the electrical power transfer to the discharge (P_w) and the mass flow ($\dot{m}$).

$$\Delta H = \frac{P_w}{\dot{m}} \tag{59}$$

The torch works with a straight annular injection. The axisymmetry of the configuration has been checked with a flow visualisation technique in cold condition [30].

Test case	Mass flow	Average total enthalpy	Pressure
C1	0.55 g/s	3.2 MJ/kg	50 mbar
C2	1.0 g/s	1.8 MJ/kg	50 mbar
C3	0.55 g/s	3.2 MJ/kg	200 mbar
C4	1.0 g/s	1.8 MJ/kg	200 mbar

Table 5 Working conditions considered in the Minitorch
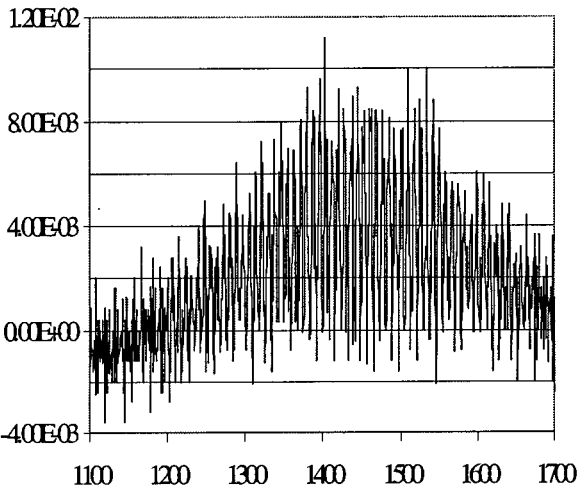
(a) Non-filtered signals
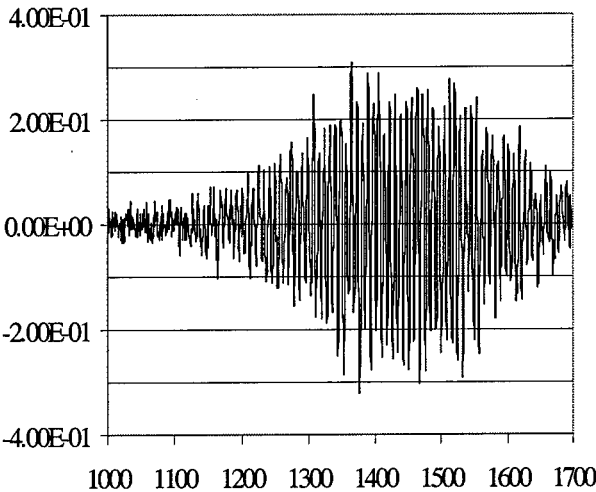
(b) Filtered signals

Figure 36 Typical Doppler signals

The LDV measurements have been implemented in the plasma jet, 20 mm downstream of the torch exit. They are taken along the radius since the axisymmetry of the jet has been checked. All the optical set-up of the LDV system is fixed to a table that can move in the three directions. In our case, the intersection of the laser beams is located on the axis of the jet (figure 37). This location is taken as marking the reference plane and the traverses are performed across the jet in that plane. The

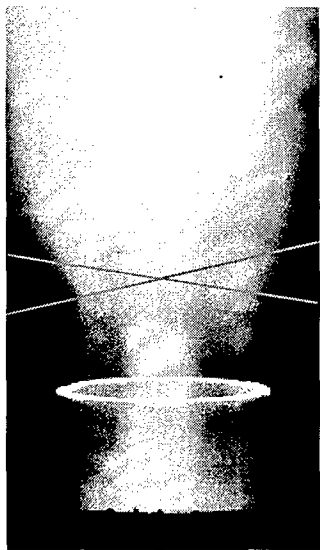position of the table is checked by a ruler which has an accuracy of half a millimetre for each displacement.

Figure 37. Crossing laser beams in the plasma jet
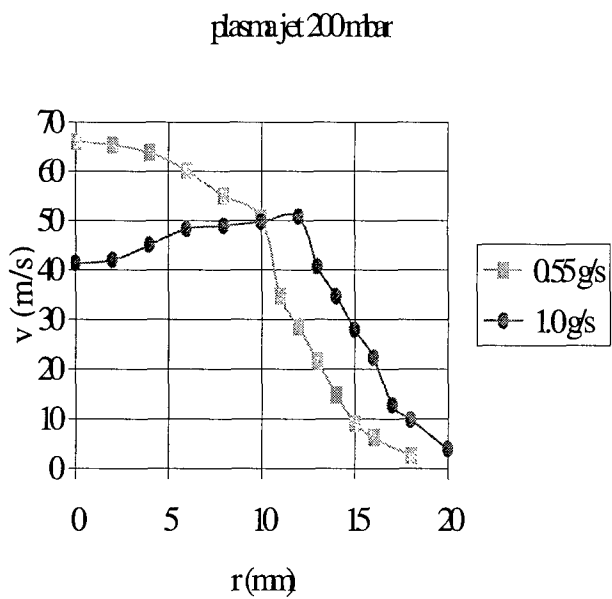
plasma jet 200mbar

Figure 38. Velocity profiles of the plasma jet, cases C3 & C4

At each step the Doppler signals are measured with an oscilloscope. The band-pass filter is chosen and we control the data rate and the validation rate. A measurement corresponds to a recording of one thousand valid signals. The velocity profiles of the plasma jet are shown in figures 38 and 39. The seeding of the plasma was performed at 200 mbar with particles of silica, less than 1 μm in diameter, and at 50 mbar, with particles of aluminium with a diameter of 5 to 10 μm.

The trends of the velocity profile for the two ranges of pressure are similar. The differences between the curves are more pronounced at higher pressure. As a result

of the coupling between the temperature and the velocity profiles in the plasma jet, the maximum velocity is decreasing when increasing the mass flow rate. For the higher-pressure ranges the velocity gradient at the border of the jet is larger than for the lower pressure cases. This is coherent with the visual inspection of the jet which appears more open at higher pressure. This corresponds to a more extended mixing layer.
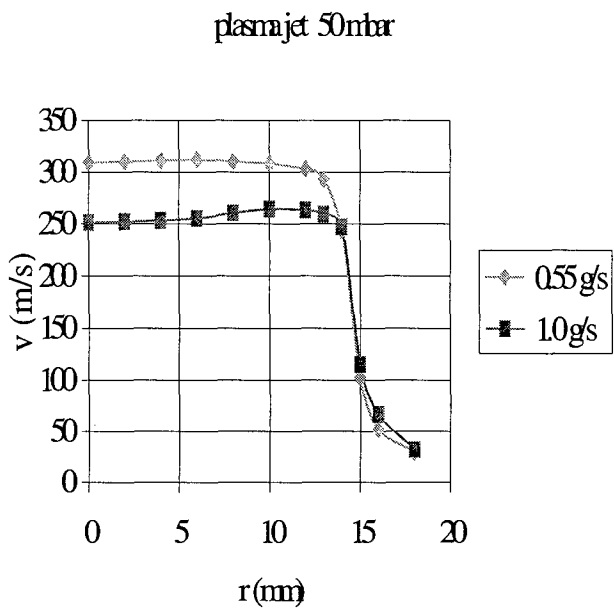
plasma jet 50mbar

Figure 39. Velocity profiles of the plasma jet, cases C1 & C2

5.3 Final remarks

As a non-intrusive and space-resolved technique, LDV measurements bring detailed information about the plasma flow. The implementation can be realised with a classical set-up using adapted interference filters. Nevertheless the seeding appears as the most important problem and has to be carefully examined to achieve accurate measurements. It can lead to some limitations because of the agglomeration and sedimentation of the particles to the tube wall. Particle evaporation in the coil region can induce plasma instabilities which drastically disturb the flow field. Once these problems are solved by selecting an appropriated seeding particle, LDV measurements provide precise results to assess the accuracy of more global high enthalpy measurement techniques, such as presented earlier in this review.

List of References

[1] CHAZOT, O.; PEREIRA GOMES, J.M.; CARBONARO, M.: Characterization of a "mini-plasmatron" facility by Pitot probe measurements. In *AIAA 29th plasmadynamics and lasers conference, AIAA paper 98-2478*, Albuquerque (USA), 15-18 June 1998.

[2] BOTTIN, B., CARBONARO, M., VAN DER HAEGEN, V., PARIS, S.: Predicted and measured capability of the VKI 1.2 MW Plasmatron regarding re-entry simulation. In *3rd European symposium on aerothermodynamics for space vehicles, ESA SP-426*, ESTEC, Noordwijk (The Netherlands), 24-26 November 1998, pp 553-560.

[3] LUMENS, J.F.; BOTTIN, B.; CARBONARO, M.: Design of a steady-state heat flux probe for measurements in an induction-heated plasma flow. In *ICIASF '97 Record (Ed. F. Kevin Owen), IEEE Publication 97CH36121*, Pacific Grove (USA), September 29 - October 2, 1997, pp 410-418.

[4] BARONETS, P.N.; KOLESNIKOV, A.F.; KUBAREV, S.N.; PERSHIN, I.S.; TRUKHANOV, A.S.; YAKUSHIN, M.I.: Overequilibrium heating of the surface of a heat-shield tile in a subsonic jet of dissociated air. *Fluid Dynamics (Soviet Research)*, **26** (3), May 1991, pp 319-476.

[5] KLINE, S.J. & MCCLINTOCK, F.A.: Describing uncertainties in single-sample experiments. *Mechanical Engineering*, **75** (1), January 1953, pp 3-8.

[6] BOTTIN, B.: Aerothermodynamic model of an inductively-coupled plasma wind tunnel. *Ph.D. Dissertation, Université de Liège & von Karman Institute for Fluid Dynamics*, October 1999.

[7] BOTTIN, B.; VANDEN ABEELE, D.; CARBONARO, M.; DEGREZ, G.; SARMA, G.S.R.: Thermodynamic and transport properties for inductive plasma modeling. *Journal of Thermophysics and Heat Transfer*, **13** (3), July 1999, pp 343-350.

[8] MACMILLAN, F.A.: Viscous effects on Pitot tubes at low speeds. *Journal of the Royal Aeronautical Society*, **58** (8), August 1954, pp 570-572.

[9] SHERMAN, F.S.: New experiments on impact-pressure interpretation in supersonic and subsonic rarefied air streams. *NACA Technical Note 2995*, September 1953.

[10] HOMANN, F.: The effect of high viscosity on the flow around a cylinder and around a sphere. *NACA Technical Memorandum 1334*, July 1952.

[11] FAY, J.A. & RIDDELL, F.R.: Theory of stagnation point heat transfer in dissociated air. *Journal of the Aeronautical Sciences*, **25** (2), February 1958, pp 73-85.

[12] ANDERSON, J.D.JR.: Hypersonic and high temperature gas dynamics. McGraw-Hill Book Company, New York, 1989.

[13] PETERS, N.: Lösung der Grenzchichtgleichungen für chemisch reagierende Gase mit einem Mehrstellenverfahren. *DLR report 72-58*, August 1972.

[14] FLETCHER, C.A.J.: Computational techniques for fluid dynamics, vol. 2. Springer-Verlag, Berlin, 1991.

[15] HOFFMANN, K.A. & CHIANG, S.T.: Computational fluid dynamics for engineers. Engineering Education Systems, Wichita, 1993.

[16] BARBANTE, P.: Chemically reacting high-temperature gas flow around a stagnation point. *VKI Project Report 1996-03*, June 1996.

[17] KOLESNIKOV, A.F.: Conditions of simulation of stagnation point heat transfer from a high-enthalpy flow. *Fluid Mechanics (in Russian)*, **1**, January 1993, pp 131-137.

[18] BOTTIN, B.; PARIS, S.; VAN DER HAEGEN, V.; CARBONARO, M.: Experimental and computational determination of the VKI Plasmatron operating envelope. In *30th AIAA Plasmadynamics and Lasers Conference, AIAA paper 99-3607*, Norfolk (USA), June 28 - July 1, 1999.

[19] VAN DEN BRAEMBUSSCHE, R.; ARTS, T.; BOERRIGTER, H.; CARBONARO, M.: Pressure Measurements. In *Introduction to Measurement Techniques, VKI Lecture Series 1994-01*, Rhode-Saint-Genèse (Belgium), (annual lecture), pp 41-138.

[20] SCHLICHTING, H.: Boundary-layer theory.
McGraw-Hill, New York, 1955.

[21] CHAZOT, O.: Global characterisation of plasma flow
in an ICP torch by intrusive measurements.
VKI Internal Note 117, June 1999.

[22] PFEIFER, H.-J.: Measurements in gas and flames.
VKI Lecture Series 1981-03, 1981.

[23] MELLING, A.: Particle behaviour in flows and
suitable particles for LDA measurements.
VKI Lecture Series 1981-03, 1981.

[24] GOUSBET, G. & TRINITE, G.: Anémométrie laser
doppler interférentielle dans une torche à plasma
haute fréquence.
J. Phys. E. Sci. Instrum., **10,** 1977, pp 1009-1016.

[25] GLASS, M. & KENNEDY, I.M.: An improved seeding
method for high temperature laser doppler
velocimetry.
Combustion and Flame, **29,** 1977, pp 333.

[26] MUNGAL, M.G.: Experiments in combustion (lecture
3).
In *Introduction to Turbulent Combustion, VKI
Lecture Series 1999-04,* Rhode-Saint-Genèse,
March 22-26, 1999.

[27] BONET, C., DAGUENET, M., DUMARGUE, P.: Etude
théorique de l'évaporation d'une particule sphérique
d'un matériau réfractaire dans un plasma thermique.
International Journal of Heat and Mass Transfer,
17, 1974, pp 643-654.

[28] GOUSBET, G.: A review on measurements of particle
velocities and diameters by laser techniques, with
emphasis on thermal plasmas.
Plasma Chemistry and Plasma Processing, **5** (2),
1985, pp 91-117.

[29] MOREAU, P. & LABBE, J.: Laser velocimetry in high
velocity combustion flow.
ONERA-TP-1978-75, 1978.

[30] CHAZOT, O.: Qualitative description of the flow field
of an ICP torch with a cold model.
VKI Internal Note 114, January 1999.